Optimized Microwave-based Synthesis of Thermally-Stable Inverse Catalytic Core-Shell Motifs for CO_2 Hydrogenation

Kenna L. Salvatore[1], Kaixi Deng[1,2], Shiyu Yue[1,⊥], Scott C. McGuire[1,⊥], José A. Rodriguez[2], and Stanislaus S. Wong[1,*]

Email: stanislaus.wong@stonybrook.edu

[1]Department of Chemistry, State University of New York at Stony Brook, Stony Brook, NY 11794-3400

[2]Chemistry Department, Building 555, Brookhaven National Laboratory, Upton, NY 11973

[⊥]These authors contributed equally to this manuscript.

*To whom correspondence should be addressed.

Abstract

The rational synthesis of Cu@TiO_2 core@shell nanowire structures was thoroughly explored using a microwave-assisted method through the tuning of experimental parameters such as but not limited to (i) controlled variation in molar ratios, (ii) the effect of discrete Ti precursors, (iii) the method of addition of the precursors themselves, and (iv) time of irradiation. Uniform coatings were obtained using Cu: Ti molar ratios of 1: 2, 1: 1, 2: 1, and 4: 1, respectively. It should be noted that whereas relative molar precursor concentrations primarily determined the magnitude of the resulting shell size, the dependence was non-linear. Moreover, additionally important reaction parameters, such as precursor identity, the means of addition of precursors, and the reaction time, were individually explored with the objective of creating a series of optimized reaction conditions. As compared with Cu nanowires (NWs) alone, it is evident that both of the Cu@TiO_2 core-shell NW samples, regardless of pre-treatment conditions, evinced much better catalytic performance, up to as much as 20 times greater activity as compared with standard Cu NWs. These results imply the significance of the Cu/TiO_2 interface in terms of promoting CO_2 hydrogenation, since TiO_2 alone is known to be inert for this reaction. Furthermore, it is additionally notable that the N_2 annealing pre-treatment is crucial in terms of preserving the overall Cu@TiO_2 core@shell structure. We also systematically analyzed and tracked the structural and chemical evolution of our catalysts before and after the CO_2 reduction experiments. Indeed, we discovered that the core@shell wire motif was essentially maintained and conserved after this high-temperature reaction process, thereby accentuating the thermal stability and physical robustness of our as-prepared hierarchical motifs.

Keywords: core-shell; copper; titania; catalysis; chemical processing; CO_2 reduction

1. Introduction

Carbon dioxide (CO_2) emanates as a byproduct of both natural and human-derived sources,[1] Therefore, an area of recent interest[2-5] concerns the conversion of CO_2 into feedstock for commodity chemicals, fuels, and materials (i.e. products with energy-dense chemical bonds) by chemical, thermal, photocatalytic, and electrocatalytic means.[6] The reduction of CO_2 to form hydrocarbons, alcohols, and similar related products can be mediated by a transition metal surface. In this respect, copper nanomaterials have been investigated for this application, due to an increased number of exposed active sites on the (110) planes, as confirmed by DFT.[7-8] The catalytic activity of Cu nanomaterials has been enhanced not only through enrichment with Au[9-10] but also through the formation of bimetallic alloys, incorporating elements such as but not limited to Bi,[11] Pt,[12] Pd,[10] and In,[10, 13] respectively. However, there are legitimate concerns more broadly about controlling (i) product selectivity and yields as well as overcoming (ii) the high overpotentials needed and (iii) the poor Faradaic efficiency observed.[14]

Copper (Cu) possesses intrinsic advantages, such as high conductivity, relative abundance, low cost, and relative non-toxicity..[15] Specifically, one-dimensional (1D) Cu nanomaterials, such as Cu NWs, are promising for their effective structural flexibility, electrical conductivity, and stability.[16] Furthermore, composites based on 1D Cu NWs possess many favorable advantages as compared with 0D Cu nanoparticles (Cu NPs), such as large surface area, reasonable surface facet control, and large contact areas associated with active sites. For example, the activity of a copper (111) surface, as a catalyst for the water-gas shift and CO_2 hydrogenation, can be increased by the addition of overlayers of ceria or zinc oxide, as a result of creating an inverse oxide/metal configuration.[17-20] These previous works have motivated our interest in the preparation and testing of Cu core@oxide shell heterostructures as catalytic

platforms. Moreover, as an added and prevailing stimulus for our reported experiments herein, one of our groups has extensively studied this hierarchical structure in the context of designing efficient catalysts for the methanol oxidation reaction and the oxygen reduction reaction.[21-28]

In this current study, as an illustrative demonstration of principle of the significance and relevance of this morphological motif for applications, we have synthesized and probed a core-shell structure, composed of a Cu NW surrounded by an outer TiO_2 layer. In general, the core-shell motif yields four primary benefits toward enhancing the intrinsic activity of catalysts. *First*, it maximizes the use of an inexpensive but still catalytically active Cu core. *Second*, the ability to tailor the size of the TiO_2 shell should enable an optimization of either chemical or catalytic reactivity. *Third*, the underlying one-dimensional, anisotropic wire structure is advantageous in that it primarily exposes the catalytically active Cu (100) facet,[29] associated with the 'long' rod portion of the nanowire.[30] *Fourth*, the core-shell structure creates a canonical metal / semiconducting metal oxide interface, which may not only enable effective interfacial charge transfer by minimizing deleterious charge recombination effects[31] but also enhance structural stability by reducing corrosive influences.[32]

Previous work on Cu@TiO_2 core-shell motifs has focused on applications, such as but not limited to H_2 conversion,[33] the photocatalytic degradation of methyl orange,[34,35] and dye-sensitized solar cells.[36] With respect to CO_2 reduction, it is important to note that essentially all of the prior studies relate to either photocatalysis or electrocatalysis, which possess a different scope from what we intend to investigate herein. In these previously reported systems, the observed activity has often correlated with shell thickness. As illustrative examples, Cu-based core@shell motifs have been generated not only with metals such as Sn[37-38] and Au but also with metal oxides including In_2O_3 and SnO_2. The efficiency and composition of syngas production on

carbon-supported Cu/In_2O_3 catalysts were highly dependent upon the In_2O_3 shell thickness (0.4 to 1.5 nm).[39] Separately, Cu/SnO_2 core-shell structures enable the electrochemical reduction of CO_2 to formate; thicker (1.8 nm) shells generate formate species, whereas thinner (0.8 nm) shells are selective to CO formation.[40] Atomic layer deposition (ALD) of SnO_2 on Cu NWs[41] was used to enhance selectivity towards producing CO. As another example, Au cubic NPs with 7-8 layers of Cu gave rise to higher selectivity towards C_2H_4 formation, whereas Au cubic NPs with over 14 layers of Cu were more selective towards CH_4 generation.[42] Differences in the observed product distribution were attributed to the compressive strain effect of the Cu overlayer in the adsorption of reactive intermediate species, with an increased Cu content favoring the 'hydrogenation pathway' of CO_2 to methane. Moreover, CuO@Cu core-shell structures were yielded Faradaic efficiencies of CO and HCOOH that were higher than those with other catalyst loadings with a short reaction time.

In stark contrast with the prior literature, we will explore the potential of novel, as-prepared $Cu@TiO_2$ NWs as thermal catalysts for which no previous precedence exists, to the best of our knowledge. Specifically, we will be analyzing the use of these materials within the context of a CO_2 hydrogenation reaction to produce CO. This process utilizes a reverse water gas shift reaction (RWGS), which requires high temperatures (400-600^{o}C). Therefore, the thermal stability of the catalyst becomes relevant and essential for ensuring effective performance.[43]

From a synthetic perspective, as a means of fabricating these motifs, groups have relied on methods, such as but not limited to standard hydrothermal, reflux, and microwave wet-chemical methods.[33,34-36, 44-45] Yet, each of these conventional protocols has certain associated limitations. Reflux methods tend to be characterized by lower yields and overall longer reaction times. Moreover, many of these syntheses often use either oleylamine or other organic

surfactants which can be difficult to remove and which otherwise passivate the surfaces of the heterostructures, thereby interfering with their observed performance.[46] With hydrothermal methods, the reaction times can often be very extensive. Indeed, conventional heating methods tend to be slower, due to their dependence upon phenomena, such as the formation of convection currents, the thermal conductivity of the materials, and the temperature of the reaction vessel itself, the latter of which often needs to be much higher than that of the reaction mixture.[47]

By contrast, microwave-based synthesis methods possess a number of advantages, including but not limited to a relatively facile procedure, ease of use, and shorter reaction times (since most reactions only take a few minutes), as compared with conventional heating techniques, all of which render the microwave procedure as potentially more amenable and accessible for industrial applicability.[47] Specifically, microwave treatments allow for a more thorough and uniform heating of the sample. Indeed, the temperature of the whole reaction volume can increase simultaneously and homogeneously, with the use of dielectric-based heating. Furthermore, microwave chemistry allows for control over a number of reaction parameters, such as power, frequency, the nature of the precursors, the surfactant, the reducing agent involved, the type of solvent, and reaction temperature.

In the context of our desired Cu@TiO_2 core-shell motifs herein, previously reported microwave methods have relied on using either $TiCl_3$[33] or TiF_4 as the titanium source, both of which are inherently hazardous precursors. Other microwave syntheses have attempted to produce Cu NWs under *in situ* conditions.[34] In the process however, the resulting shell size of the core@shell structure has been very difficult to tune and tailor. The use of long reaction times has meant that the isolated product architecture is sensitive to moisture contamination. As such, in terms of novelty, we have put forth a number of key synthetic advances. *First,* we have adapted

microwave-based synthesis using a safer precursor molecule, i.e. titanium butoxide, TBOT, in the context of a water and surfactant-free methodology. *Second*, we have adjusted reaction parameters, such as precursor amounts and reaction time, as a means of controllably tuning shell thickness and customizing shell uniformity around the underlying Cu NW without degrading it.[33]

In this paper, we have sought to generate a tailorable Cu@TiO_2 core@shell nanowire structure with tunable outer shell radii, in which the specific effects of synthetic processing parameters, such as metal precursors, solvents, reaction time, and reaction temperature, have been individually probed and correlated with CO_2 reduction performance. What we have found is that (i) the ensuing morphology (i.e., the core-shell architecture) and (ii) chemical processing treatments make a substantive difference with respect to assessing the resulting thermal CO_2 reduction catalytic performance. In fact, we determined that performance levels may achieve levels as much as 20 times greater activity as compared with standard Cu NWs.

2. Synthesis and Characterization

2.1. Materials

Materials were used as received, including $CuCl_2$•$2H_2O$ (Baker Analyzed), D-glucose (anhydrous) (Fisher Scientific, Certified ACS), 1-hexadecylamine (Acros Organics, 90%), titanium butoxide (TBOT) (Acros Organics, 99%). Anhydrous ethanol (Beantown Chemical, denatured), n-hexane (Alfa Aesar, Spectrophotometric grade, 95+%), chloroform (Alfa Aesar, ACS, 99.8%), and DI water were all utilized as procured, without any additional purification protocols involved.

2.2. Experimental: Copper Nanowires

Cu nanowires were first synthesized using a previously published method.[30] That is, the wires were produced hydrothermally. For this synthesis, 1.08 grams of $CuCl_2$•$2H_2O$ (copper

source), 7.20 grams of 1-hexadecylamine (capping agent), and 2.14 grams of D-glucose (reducing agent) were added to 400 mL of water and then stirred for over 12 hours overnight, until the solution turned into a light blue emulsion. Subsequently, the solution was added into a Teflon autoclave, and then heated to 100^{o}C for 12 hours. The wires are then thoroughly washed several times via centrifugation with a combination of hydrophilic solvent (water) and hydrophobic solvent (chloroform/hexane) to simultaneously remove particles and excess 1-hexadecylamine. The resulting wires possessed average diameters in the range of 20 to 50 nm with lengths of microns. The Cu NW products could be indexed as the *fcc* phase (JCPDS #03-1018) of pure copper, as corroborated by the XRD results. These data are characterized by a high-intensity [111] facet (shown in the XRD peak and located at ~43^{o}) coupled with a high-intensity [200] facet (highlighted at 50.5^{o}) (Figure S1).

2.3. Synthesis of Cu/TiO_2 Core shell structures

This work was adapted from and builds upon a previously published study, which reported on the fabrication of Cu metal core@shell metal oxide structures.[33] These motifs were produced using microwave synthesis as a means of immobilizing crystalline TiO_2 structures onto an underlying copper nanowire platform. This current study differs from the previously reported methodology in the following three significant points. Specifically, we have (a) substituted water with absolute ethanol, (b) replaced the original $TiCl_3$ precursor with a safer analogue, i.e. titanium butoxide (TBOT), and (c) systematically varied the amount of TBOT as a means of correspondingly altering the shell diameter.

In practice, Cu NWs (10 mg, 0.15 mmol) were added to 4 mL of absolute ethanol (AETOH) and sonicated, until these were properly dispersed. Typically, titanium butoxide (TBOT, 0.1 mL, 0.3 mmol) was added to 1 mL of AETOH, and the mixture was sonicated, until

it yielded a clear hue. Subsequently, the TBOT solution was added in slowly, dropwise to the Cu NW solution. The resulting mixture was then further sonicated for a period of 15 to 20 min, and later heated via microwave radiation at 150^{o}C for 30 min with a pressure and power limit of 200 psi and 300 W, respectively. After cooling to room temperature, the sign of a successful reaction was the appearance of a reddish-white solid within an orange solution. Next, the solution was processed by centrifugation, and the isolated precipitate was subsequently washed with ethanol.

2.4. Instrumentation

XRD: Samples were prepared by dispersing the materials in ethanol and then drop-casting onto a zero-background holder (MTI Corporation, zero diffraction plate for XRD, B-doped, p-type Si, measuring 23.6 mm in diameter by 2 mm in thickness). Diffraction pattern data were obtained on a Rigaku Miniflex diffractometer, operating in the Bragg configuration characterized by Cu Kα1 irradiation (λ = 1.54 Å). Data were collected in the range of 20° to 80° at a scanning rate at 20° per minute.

TEM imaging: The morphology of as-prepared core/shell samples was characterized using a JEOL 1400 transmission electron microscope, equipped with a 2048 × 2048 Gatan CCD camera and operated at an accelerating voltage of 120 kV. Samples were prepared by dissolving powder samples in ethanol followed by drop casting onto a copper grid.

SEM imaging: An ultra-high-resolution field emission Hitachi 4800 scanning electron microscopy was employed to characterize the apparent morphology of as-prepared core/shell structures. Samples were generated by dissolving powder samples in ethanol followed by drop casting aliquots onto a silicon wafer.

HRTEM: HRTEM images were collected on a JEOL 2100F instrument, which had been operating at accelerating voltages of 200 kV with a beam size of 2 Å. Samples were prepared by

dissolving powder samples in ethanol, followed by drop casting onto a copper grid.

X-ray Near Edge Fine Structure Spectroscopy (XANES)

The XANES spectra of the Cu and Cu@TiO_2 nanowires were collected at the 8-ID Inner-Shell Spectroscopy (ISS) (Cu *K*-edge) and the 7-BM Quick X-ray Absorption and Scattering (QAS) (Ti *K*-edge) beamlines of the National Synchrotron Light Source II (NSLS-II), at Brookhaven National Laboratory (BNL). In these tests, powder samples were loaded into a quartz tube with 1.0 mm outer diameter (OD) and 0.9 mm inner diameter (ID). The Cu *K*-edge and Ti *K*-edge XAS spectra were collected in the fluorescence-yield mode and then calibrated using Cu foil and Ti foil as standards, respectively.

2.5. Catalytic activity measurements

The catalyst was pre-treated using two different regimes. (1) For samples labeled as "without N_2 annealing": Samples were treated in 10 sccm (standard cubic centimeters per minute) of 10 vol % O_2 / N_2 at 350°C for 1 h with a ramping and cooling rate of 10°C/min to remove adventitious carbon emanating from the synthesis process from the surfaces of the catalysts. (2) For samples, labeled as "N_2 annealed": These samples were treated step-wise in N_2 at 450°C, 10 vol% O_2/N_2 at 350°C, and ultimately, 50 vol% H_2/N_2 at 450°C, for periods of 1 h at each temperature with ramping and cooling rates of 10 °C/min.

For the activity measurements, 1-2 mg of samples were loaded into a quartz capillary measuring 0.9 mm in internal diameter with a fixed gas flow of 2 sccm CO_2, 2 sccm N_2, and 6 sccm H_2 applied with 16-18 psi pressure. Catalytic activities were measured, stepwise, at 250°C, 350°C, and 450°C with a ramping rate of 10°C/min. The reaction vessel was held at each temperature for 80 min at each temperature. The concentrations of gases evolved were analyzed

with a gas chromatography instrument (Agilent 7890A), equipped with both flame ionization and thermal conductivity detectors. The N_2 in the gas flow was used as an internal standard.

$$\text{CO space time yield } \mu\text{mol}*(s*g_{Cu})^{-1} = f_{CO} * \frac{1}{m*Cu\ wt\%} * \frac{f_{N_2}(\text{RT})}{f_{N_2}(\text{rxn})} * 10 * 7.45 * 10^{-1} \frac{\mu mol}{s}$$

wherein 1 sccm = $7.45*10^{-7}$ mol/s; m = sample mass (g); Cu wt% = weight percent of Cu in catalyst; f_{CO} = volume concentration of the CO gas in the outlet; $f_{N_2}(\text{RT})$ = volume concentration of N_2 in the outlet measured at room temperature; and $f_{N_2}(\text{rxn})$ = volume concentration of N_2 in the outlet measured under the relevant reaction conditions.

3. Results and Discussion

3.1. Insights into Synthesis Mechanism

The efficiency of microwave synthesis depends on a number of different, distinctive variables. First, the effectiveness of the solvent can be characterized by the loss tangent parameter (tan δ), which represents the materials' inherent dissipation of electromagnetic energy. A large loss tangent value implies a higher absorption of energy, whereas a low loss tangent number is indicative of a lower and slower absorption of energy. The magnitude of the loss tangent is affected by solvent polarity, a variable which governs the extent to which the solvent interacts with the microwaves.[47] Whereas prior synthesis methods utilized water (tan δ = 0.123), we chose to use absolute ethanol, so as to not oxidize the Cu NWs. This solvent possesses a higher tangent loss parameter of 0.941, suggesting that the solvent will exhibit an increased microwave absorption capability, a characteristic which will necessarily impact upon observed reaction rates and consequentially increase temperatures more rapidly within the medium.[48]

Role of Ti precursors: Bulk TiO_2 was initially used with a 1: 1 Cu: Ti precursor ratio, and these

reagents were reacted at 150^{o}C for 30 minutes. However, this process resulted in not only in an undesired aggregation of as-formed TiO_2 nanoparticles but also an overall lack of uniform coverage of these particles onto the external surfaces of these underlying Cu NWs, likely due to the relatively poor hydrolysis and solubility of TiO_2 at room temperature. This situation was presumably responsible for the lack of ionization and the concomitant inadequate dispersion of Ti ions within the solution, as indicated by our SEM results (Figure S2).[33] Moreover, the data in Figure S2 imply that the resulting TiO_2 'layer' actually consists of relatively large, ~100-200 nm particulate motifs, which do not homogeneously coat the Cu core in any uniform manner.

Titanium butoxide (TBOT) was subsequently utilized, due to its key tendency to hydrolyze in water and other polar solvents at room temperature. A prior study reported that as compared with other precursor Ti sources (such as $TiCl_4$ and $Ti(SO_4)_2$), the use of TBOT led to the best photocatalytic performance observed.[49] In part, this observation can be attributed to the finding that TBOT, which is relatively uniformly dispersed in absolute ethanol, forms a Ti-hydroxide solution which not only (1) slows down the hydrolysis of Ti in solution but also (2) allows for the homogeneous dispersion of Ti ions within the reagent solution. Once sonication begins, the $Ti(OH)_x$ molecules likely attach onto the surfaces of the underlying Cu NWs through the formation and precipitation of amorphous TiO_2 during the microwave heating process.[50]

Role of Reaction Time: In order to fully understand the mechanistic process underlying the microwave irradiation process, we also probed and correlated the impact of varying irradiation time (i.e., 10 to 40 minutes) upon the resulting sample morphology (Figure S3). Specifically, a sample generated with too little reaction time yielded a product characterized by an uneven coating (Figure S3A-D). By contrast, the use of an excessive reaction time led to wire degradation into smaller constituent particulate bits (Figure S3G). Based on all of our

experiments, the ideal reaction time necessary to generate a relatively monodisperse, homogeneous, and uniform coating was in the range of 30 to 35 minutes (Figure S3E-F).

Role of Precursor Addition Methodology: After the reaction time was optimized, we further improved upon the quality of the as-deposited coating by exploring the effect of precisely *how* the Ti precursor was introduced into the reaction medium. Specifically, we noted that when TBOT was initially solubilized and dispersed in absolute ethanol prior to addition with Cu NWs, the coating became much more regular and consistent (Figure S4B) as compared with the product obtained from the simple, direct addition of TBOT (Figure S4A).

As such, we collected experimental XRD patterns of both samples, and confirmed that the sample derived from the straight addition of the TBOT precursor in the presence of Cu NWs gave rise to significantly higher Cu_2O and CuO impurities. This finding is most likely attributable to the relatively uneven coverage of TiO_2 which left segments of the Cu NWs exposed to air, thereby resulting in the observed oxidation both during and after the reaction process. By contrast, when we solubilized and dispersed TBOT in absolute ethanol and added that solution in dropwise to the Cu NW-containing reaction medium, the TBOT precursor was found to have more evenly and uniformly coated the Cu surface. XRD analysis of this latter sample was consistent with the lack of any apparent copper oxide impurities.

3.2. Characterization of as-prepared Cu@TiO_2 core@shell nanowire motifs:

The XRD pattern of the as-generated optimized material, produced with a 1: 2 Cu: Ti molar ratio and denoted as **1Cu@2TiO_2** (Figure 1A), highlighted three distinctive peaks, which could be attributed to Cu (JCPDS #03-1018), coupled with a highly amorphous region near the beginning of the XRD pattern.[33] However, the ostensible lack of TiO_2 peaks is not surprising, given the amorphous nature of the titania shell surrounding the copper core. While no TiO_2 peaks

are definitively apparent, slight imperfections, localized not only on the third peak of Cu but also at ~35-40^{o}, could potentially be assigned to anatase TiO_2.[33] We also did not observe any crystalline copper oxide (i.e., either CuO or Cu_2O). It is possible that these species might exist either in an amorphous form or in insufficiently small quantities to have clearly shown up on XRD. However, based on our collective results (including but not limited to Figure S4), if there had been a large amount of copper oxide present, it would have been apparent in the XRD data. As determined from the SEM and TEM images presented in Figure 1B-E, the shell size was measured to be 37.3 ± 8.0 nm. The shell composition consisted of an anatase phase of TiO_2. Specifically, from HRTEM, the indexed d_{101} plane ascribed to anatase TiO_2 measured roughly 3.7 ± 0.5 Å. We note that the individual underlying Cu planes themselves were likely too obscured by the thick TiO_2 shell in order for them to be precisely determined and indexed.

Further chemical characterization was explored, and SEM-EDX data were taken on the samples as well. In particular, EDX data were acquired on both 'point' and 'box' regions for a total of 5 data sets (Figure 2 and Figure S5). That is, we were able to obtain SEM-EDS data at 5 different regions, scattered across the sample so as to provide a representative idea of elemental distributions. We define a 'point' as corresponding to a singular position on an individual wire, whereas a 'box' refers to either the entire image or a map encompassing many wires. All of these data indicate essentially identical results, with high amounts of Ti observed coupled with lower amounts of Cu detected on the external sample surface, thereby underscoring the validity of our conclusions. Quantitatively, it should be noted that EDX analysis demonstrated both Cu (19.1 %) and Ti (80.9 %) within a ~5: 1 Ti: Cu atomic ratio. These data were therefore consistent with a comparatively thicker outer coating of TiO_2, circumscribing the inner Cu wires (Table S2).

3.3. Morphological and Chemical Composition Studies of As-prepared Cu@TiO_2

Core@Shell Motifs, Prepared with Variable Diameter

To further tune the thickness of the TiO_2 'shell', the overall precursor concentrations associated with the relative ratio of Cu: Ti were also varied (Figure 3). Specifically, the amount of precursor was systematically altered from the starting Cu: Ti molar ratio of 1: 2, for which 0.1 mL of TBOT was utilized, onwards to 1: 1, to 2: 1, and finally onto 4: 1 Cu: Ti, respectively. This set of experiments was completed by deliberatively modulating the volume of TBOT added into the solution mixture from 0.1 mL onwards to 0.05 mL (Figure 3 A, D, G, J), 0.025 mL (Figure 3B, E, H, K), and ultimately to 0.0125 mL (Figure 3 C, F, I, L), respectively, while maintaining reaction time, reaction temperature, and the relative amount of Cu as constants.

We should note that a core@shell structural motif successfully formed after each experimental run. Initially, the amount of TBOT was halved from 0.1 mL to 0.05 mL to provide for a 1: 1 molar ratio between Cu and Ti. This move resulted in the measured dimension of the TiO_2 shell decreasing from 37.3 nm to 28.4 ± 5.7 nm, as indicated by the purple bracket within Figure 3G. It was noted that the shell appeared to be homogeneously dispersed on the surface of the copper nanowires, as observed from the SEM and TEM images (Figure 3A and 3D). The corresponding lattice *d*-spacing values were determined for the Cu d_{111} and TiO_2 d_{101} data to be 2.1 ± 0.1 Å and 3.3 ± 0.4 Å, respectively, as shown in Figure 3J. The quantity of TBOT was then halved again to 0.025 mL TBOT to yield a 2: 1 Cu: Ti molar ratio. This latter step decreased the apparent shell size further to 19.1 ± 5.7 nm, as highlighted by the purple bracket in Figure 3H. The corresponding lattice *d*-spacing data were consistent with Cu d_{111} and TiO_2 d_{101} values of 2.0 ± 0.1 Å and 3.5 ± 0.4 Å, respectively, as shown in Figure 3K. An additional HRTEM image that reinforces these findings is shown in Figure S6. Finally, the TBOT amount was further halved yet again to 0.0125 mL to provide for a final molar ratio of 4: 1 Cu: Ti. It should be noted that

the apparent titania shell size appeared to have been reduced to 10.7 ± 3.0 nm, which was about 4x smaller in dimension than the original 37 nm motif, as outlined by the purple brackets in Figure 4I. From the corresponding HRTEM data, the Cu d_{111} and TiO_2 anatase d_{101} values were indexed to be 2.1 ± 0.1 Å and 3.0 ± 0 3 Å, respectively (Figure 3L).

All of the information provided above has been summarized and tabulated in Table 1. By systematically decreasing the amount of TBOT at 'set' quantities, the shell size correspondingly decreased by ~10 nm, each time (Table 1). The indexed Cu core reading measured ~2.0 Å, associated with the (111) plane. The analogous (101) anatase TiO_2 plane remained at ~3.3 nm, although there did appear to be a slight downward trend and contraction in the lattice spacing with decreasing titania shell size, perhaps due to a compression-like strain effect induced upon the monolayer-like shell as a result of the underlying Cu(110) core.[51] With respect to the shell size, the decrease in size correlated in a non-linear fashion with molar titania precursor concentration, as shown in Figure 4. This denotes an important finding for future work with respect to tailoring metal/semiconducting core@shell structures.

4. CO_2 Hydrogenation Performance

4.1. Catalytic Performance of Samples Processed by Annealing *with* N_2 Treatment

To test the activity of our as-prepared nanomaterials for CO_2 hydrogenation, samples incorporating 1: 2 and 2: 1 Cu: Ti molar ratios were tested. These samples were denoted as **1Cu@2TiO₂** and **2Cu@1TiO₂ O₂**, respectively (Figure 1 and Figure 3B). Nevertheless, to remove any adventitious carbon which might have interfered with catalytic performance, the sample had to undergo a series of distinctive annealing regimes. As an *initial first step*, the samples were first annealed under N_2 at 450^{o}C for one hour to more effectively crystallize and

stabilize the intrinsic core@shell morphology (Figure 5A and B). The morphology was conserved, and significantly, the measured shell size did not appear to have been affected by this treatment for either of the molar ratios (Figure 5A and B, Table 2). By contrast, we noted an increase in crystallinity of the TiO_2 shell as compared with the amorphous pristine sample.[52] We can postulate the formation of the anatase phase of TiO_2, due to the annealing process at 450^oC.

In the *second step* of the process to remove excess carbon, the sample underwent O_2 treatment at 350^oC for one hour. Likewise, this process did not damage the sample morphology for either shell size (Figure 5C and D). As a *final step*, to reduce the sample back to Cu^0, the sample underwent H_2 treatment at 450^oC for one hour (Figure 5E-F). Overall, over the course of the entire annealing protocol, the TiO_2 increased in crystallinity, evolving from an amorphous to a crystalline state. Furthermore, the overall radius of the shell was conserved (i) at ~35 nm for the **1Cu@2TiO$_2$** sample, and (ii) at ~20 nm for the **2Cu@1TiO$_2$** sample, respectively (Figure 5, Table 2). From the TEM data, the annealing protocol appeared to have rendered the latter **2Cu@1TiO$_2$** sample as perceptibly more porous in nature, presumably due to a lack of sturdiness of the shell coating, owing to its inherent thinness.

To investigate how the pre-treatment processes affected the preservation of the core-shell structure, XANES measurements were carried out on samples which had been treated under different annealing conditions. Since the transition from bulk, amorphous TiO_2 into its crystalline analogue occurs above 350°C, a N_2 annealing step at 450°C would likely have converted amorphous TiO_2 into crystalline anatase.[52] Furthermore, as Figure 6B (red) shows, the Cu speciation within the **1Cu@2TiO$_2$ N$_2$ (red)** sample likely converted to typical metallic elemental copper. As compared with the XANES of **pristine 1Cu@2TiO$_2$** (Figure 6B, black) itself, the measured Cu signal consists primarily of Cu^{2+}, due to the presence of its characteristic feature

located at ~8978 eV in the Cu *K*-edge XANES region. However, as compared with the CuO standard, the weak 8986 eV feature in the pristine sample indicates that the Cu^{2+} is not situated within a typical CuO environment (Figure S7). When the annealed sample was oxidized, as per the **1Cu@2TiO$_2$ N$_2$, O$_2$ (blue)** sample, a CuO feature was observed (Figure 6B, blue). Subsequently, after the H_2 treatment, Cu was reduced into the expected metallic elemental copper, as shown with **1Cu@2TiO$_2$ N$_2$, O$_2$, H$_2$** (Figure 6B, green). Under either pure H_2 or CO_2 hydrogenation conditions, the results of XANES indicated that the active phase of these catalysts consisted of metallic copper in contact with anatase (Figure S8).

The catalytic activities of the 1Cu@2TiO_2, 2Cu@1TiO_2, and standard Cu NW controls, respectively, for the CO_2 hydrogenation reaction run at 350°C and 450°C are shown in Figure 6A. No activity was perceived when running the reaction at 250°C. The observed activity is shown in the context of a CO space time yield, as it was the only detected product, thereby highlighting that our as-prepared NW motifs maintain good selectivity. By comparison with the catalytic activity of Cu NWs, bulk Cu powder (150 mesh) was also tested. However, this bulk sample was so inactive, that its CO production could not even be quantified. The improved catalytic activity of our Cu NWs could be explained by their distinctive anisotropic morphology. Specifically, as opposed to commercial Cu powder, the primary exposed facet within Cu NWs consists of the catalytically active Cu(100) facet.[29-30] Therefore, as compared with Cu NWs alone (Figure 6A, red), it is evident that both of the Cu@TiO_2 samples, regardless of either molar ratio or temperature, evinced much better catalytic performance, thereby implying the significance of the Cu/TiO_2 interface in terms of promoting CO_2 hydrogenation, since TiO_2 alone is known to be inert for this reaction.[53]

If we more explicitly compare the measured performance at 350^{o}C and 450^{o}C, we find

that over that temperature range, the **1Cu@2TiO$_2$** sample increased in activity from 7.4 μmol/(g_{Cu}s) to 44 μmol/(g_{Cu}s) (Figure 6A, purple and Table 3), i.e. increasing by seven-fold. The corresponding activity of the analogous **2Cu@1 TiO$_2$** sample increased by ten-fold, i.e. rising from 2.8 μmol/(g_{Cu}s) to 27 μmol/(g_{Cu}s) (Figure 6A, green and Table 3). By contrast, the Cu NW control sample at 450^{o}C yielded only 4.9 μmol/(g_{Cu}s). It is therefore evident that the activities of the **1Cu@2TiO$_2$** sample and the **2Cu@1TiO$_2$** sample, both generated with N_2 annealing, were 10-fold and 5.5-fold higher, respectively, than that of the Cu NW sample alone. Furthermore, it is noteworthy that the production of CO observed over the entire range of all of these catalysts remained relatively constant, even after 90 minutes of reaction time (Figure S9 and Table S3). Collectively, these findings indicate that these systems represent relatively inexpensive, catalytically active, and stable architectural platforms for thermal reduction.

To further highlight the promising potential of our as-produced core-shell motifs, we should also emphasize that our **1Cu@2TiO$_2$** sample exhibited not only an observed, enhanced activity within the context of each pre-treatment condition but also, crucially, an impressive thermal stability for a core@shell NW structure. In particular, from TEM analysis, we found that after the CO_2 reduction process, the **1Cu@2TiO$_2$** sample maintained the core@shell structural motif (Figure 5H), whereas the **2Cu@1TiO$_2$** analogue was characterized by discrete, isolated islands of TiO_2 nanoparticles on the material's surface, after the reaction process (Figure 7G). Indeed, with the **2Cu@1TiO$_2$** sample, the implication is that as compared with its **1Cu@2TiO$_2$** counterpart, proportionally larger areas of the underlying Cu NW core were exposed to the reaction medium (Figure S10) and subsequently degraded, thereby suggesting that not all of these core@shell nanowires survived the CO_2 reduction process and accounting for the observed decrease in activity (Table 3, Figure 6A).

4.2. Catalytic Performance of Samples Processed by Annealing *without* N_2 Treatment

The addition of an initial N_2 annealing step preserved the initial intrinsic core-shell motif in terms of morphology and chemical composition. By contrast, in the *absence of an annealing step*, different behavior was observed (Figure 8). That is, *without* the prior crystallization of the TiO_2 shell induced by N_2, the subsequent utilization of O_2 heat treatment of the core@shell nanowires resulted in an apparent leaching of the inner core Cu NW into its outer TiO_2 shell, as highlighted by a combination of TEM and HRTEM images (Figure 7A and B).

One consequence of this leaching process was that the Cu NW decreased in size with a concomitant increase in shell thickness. Specifically, with the O_2 heat treatment, from the TEM data (Figure 7), the **1Cu@2TiO$_2$** sample expanded by as much as 10 nm in radius (Table 2) with a similar (albeit smaller) quantitative increase in shell thickness, observed with the **2Cu@1TiO$_2$** sample (Figure S11A and B). This ostensible leaching of the Cu 'core' into the TiO_2 'shell' was further corroborated through elemental TEM-EDAX analysis. In terms of elemental distribution, the sample after an O_2 heat treatment was typified by a comparatively uniform and homogeneous dispersion of not only Cu (Figure 7E) but also Ti and O (Figure 7F-G), evenly spread throughout the entire structure, as noted by the overlay in Figure 7D. Additionally, from the TEM data (Figure 7A and B), the inherent core@shell structural motif is essentially conserved, after this annealing treatment. However, samples isolated after the final H_2 treatment appeared to maintain islands of Cu NPs scattered atop the core@shell motif, as noted by TEM data (Figure S12).

Again, XANES measurements were acquired to understand the nature of these changes. In the absence of N_2 annealing, similar Cu *K* edge results were observed for the oxidized **1Cu@2TiO$_2$ O$_2$** system in Figure 9B (red). Based on our combined TEM-EDS data of **1Cu@2TiO$_2$ O$_2$**, it is likely that the Cu species dispersed throughout the entire nanowire upon

oxidation at 350°C. In the final reduction step as noted with **1Cu@2TiO2 O_2, H_2**, the Cu likely was converted into metallic Cu, thereby accounting for the generation of numerous, isolated Cu particulate islands atop the underlying nanowire surface. A comparison of the line-shape changes in Figures 6B and 9B shows that the formation of an anatase phase after pre-heating in N_2 does affect the behavior of the Cu, and thus it is not surprising that different surface morphologies are observed in the TEM images for the two types of samples.

Furthermore, after the CO_2 reduction reaction itself, the prevailing architectural motif for both the **1Cu@2TiO_2** sample (Figure 8A and B; Table 2) and the **2Cu@1TiO_2** sample (Figure S11C and D; Table 2) was that of Cu nanoparticulate islands, that had aggregated, interspersed, and immobilized onto the underlying 1-D Cu core-TiO_2 shell platform motif with radii that were comparable to those of their unreacted counterparts. What is significant is that the core@shell wire motif was essentially maintained and conserved. We also did not observe any porous substructure within the shell of the sample, as was characteristic of the N_2 annealed samples. Moreover, the TEM-EDAX analysis suggested that the Cu signal was associated not only with the particles resting atop of the TiO_2 shell (Figure 8D) but also with the central nanowire core region (Figure 8E). In addition, the O and Ti signals were still dispersed throughout the core@shell nanowire architecture (Figure 8F and G). Nevertheless, what is worth highlighting is that the **1Cu@2TiO_2** sample gave rise to appreciably greater quantities of well-defined Cu NPs atop the underlying core@shell motif, an observation which apparently correlated with improved CO_2 reduction activity. In effect, this sample gave rise to an increased catalytic activity relative to the **2Cu@1TiO_2** sample under identical reaction conditions.

Hence, without any prior N_2 annealing, the combination of TEM and EDS data confirmed that the **1Cu@2TiO_2** sample (Figure 8) was characterized by an abundance of presumably

catalytically active, well-defined 50-70 nm Cu NPs, seemingly sprinkled onto the underlying core-shell platform motif. The overall architectural structure was apparently conserved during the CO_2 hydrogenation process. By contrast, even though the overall core-shell motif was also retained, the analogous **2Cu@1TiO$_2$** sample *without* any prior N_2 annealing (Figure S11) exhibited a more disordered, irregular-looking, roughened, and less well-defined architecture.

The measured catalytic activities of the **1Cu@2TiO$_2$, 2Cu@1TiO$_2$**, and standard Cu NW control samples without any prior N_2 treatment, respectively, for the CO_2 hydrogenation reaction run at 350°C and 450°C are shown in Figure 9A. As with the data series analyzed earlier in the presence of N_2 annealing, both Cu@TiO_2 samples generated in the absence of N_2 annealing exhibited improved catalytic performance, relative to the Cu NW control, thereby reinforcing the significance of the Cu/TiO_2 interface within the core-shell motif in terms of promoting CO_2 hydrogenation, since TiO_2 alone is known to be inert for this reaction.

If we more explicitly compare the measured performance at 350^{o}C and 450^{o}C, the activity increased with temperature (i) from 11 μmol/(g_{Cu}s) to 82 μmol/(g_{Cu}s) for the **1Cu@2TiO$_2$** sample and (ii) from 6.8 μmol/(g_{Cu}s) to 45 μmol/(g_{Cu}s) for the **2Cu@1TiO$_2$** sample, respectively. These values were far better than those of the Cu NW control, in fact as much as 20 times greater. As suggested earlier, we can hypothesize that the **1Cu@2TiO$_2$** motif performs better than the **2Cu@1TiO$_2$** motif, most likely due to increased numbers of Cu NPs localized on the outer surface of the core@shell nanowire platform. We should also note that the **1Cu@2TiO$_2$** sample prepared <u>without</u> any N_2 annealing revealed an almost two-fold increase in CO_2 reduction performance as compared with its counterpart that had been undergone an N_2 annealing treatment. We can attribute that finding to structural integrity arguments. For example, the **2Cu@1TiO$_2$** sample prepared <u>without</u> any N_2 annealing appeared to have been more robust

than its analogue which had undergone N_2 treatment, because the former hardly displayed any perceptible physical degradation after the CO_2 reaction process (Figure S4). It is important to stress that within these samples, the results of XANES analysis indicate that the active phase always contained metallic copper and TiO_2. Thus, the changes in activity could be reliably ascribed to variations in the morphology and not to the chemical state of the catalysts.

4.3. Summary of Findings

As such, based on these collective data, the observed morphology of the samples, especially post-reaction, obviously matters in dictating performance. For example, TEM images showed that the **1Cu@2TiO$_2$** sample motif, which had undergone N_2 annealing, was maintained after the reaction, whereas the **1Cu@2TiO$_2$** sample, prepared in the absence of N_2 annealing, looked very different after the reduction process. Not surprisingly, their activities were dissimilar, as shown in Figure 6 and 9. We can attribute this finding to the increased amounts of exposed, active Cu sites and species, which was a consequence of Cu leaching from the core leading to the formation of Cu NPs on the external surfaces of the core@shell motif, within samples, prepared in the absence of any N_2 annealing.

What our XANES data suggest overall is that the N_2 annealing process at 450°C is expected to have converted amorphous TiO_2 into anatase, and thereby precluded the subsequent possibility of Cu dispersibility. Therefore, without Cu forming islands of reactivity on the core-shell motif surface, the Cu, localized within the core area, likely remained encapsulated by TiO_2 even after the reduction process, a statement consistent with our TEM results. With respect to the poorer outcomes observed with the **2Cu@1TiO$_2$** samples in general, this observation could

likely be ascribed to the relative lack of robustness of the shell coating during the annealing process, owing to its intrinsic narrow thinness.

Moreover, the stability of the catalysts was assessed at 450°C (Figure S9). All of these catalysts yielded a stable CO production for 80 minutes, evincing reasonable stability (with quantitative data shown in Table S3). In general, catalysts subjected to a N_2 pre-treatment gave rise to lower overall CO production with the $2Cu@1TiO_2$ sample in particular exhibiting the lowest yield at ~26 $\mu mol*(s*g_{Cu})^{-1}$. Interestingly, the $1Cu@TiO_2$ sample that had undergone an N_2 pre-treatment evinced a very similar CO production to that of the $2Cu@1TiO_2$ catalyst which, by contrast, had not experienced any N_2 pre-treatment at all, with measured yields of ~45 $\mu mol*(s*g_{Cu})^{-1}$. The best performing catalyst, namely the $1Cu@2TiO_2$ catalyst with an O_2 treatment, yielded the highest CO production observed within the series of samples we tested, i.e. ~83 $\mu mol*(s*g_{Cu})^{-1}$. Clearly, the pre-treatment protocol had an effect on the observed activity but did not impact upon the overall durability. Overall, these data suggest that the Cu/TiO_2 NW motif represents a promisingly viable and stable material for thermal catalysis[43] in terms of effectively generating CO from CO_2 at high temperatures.

5. Conclusions

A core/shell Cu/TiO_2 motif was successfully synthesized using a novel microwave-based technique, in which the effects of specific experimental parameters such as irradiation time were systematically explored and optimized. As deduced from a series of HRTEM images, it was determined that the TiO_2 shell dimension was primarily altered by changing the corresponding quantity of TBOT precursor used. The chemical composition was verified using a combination

of XRD, XPS, and SEM-EDX results, whereas the observed morphology was ascertained with structural characterization data acquired from both SEM and HRTEM measurements.

As implied earlier, a 'good' catalyst for CO_2 hydrogenation should be able to efficiently activate both CO_2 and H_2.[54] However, according to theoretical studies, while the Cu surface can effectively dissociate H_2 under elevated temperatures,[55] it is not useful in terms of activating CO_2 itself.[56] By contrast, TiO_2 activates CO_2[57] but does not dissociate H_2.[58] Hence, incorporating and combining these two components within one integrated Cu@TiO_2 core-shell structural unit ensures that both reactants are activated, thereby resulting in its much higher observed catalytic activity as compared with either constituent material alone.

In addition, we also systematically analyzed and tracked the structural and chemical evolution of our catalysts before and after the CO_2 reduction experiments. Indeed, we discovered that the core@shell wire motif was essentially maintained and conserved after this high-temperature reaction process, thereby accentuating the thermal stability and physical robustness of our as-prepared hierarchical motifs. Moreover, both of the Cu@TiO_2 samples, regardless of pre-treatment conditions, yielded a much higher catalytic performance as compared with Cu NWs alone, thereby underscoring the significance of the Cu/TiO_2 interface for promoting CO_2 hydrogenation. What is also worth emphasizing is that the 1:2 Cu: Ti molar ratio sample gave rise to appreciably greater quantities of well-defined Cu NPs atop the underlying core@shell motif, an observation which apparently correlated with CO_2 reduction activity. In effect, this sample generated increased catalytic activity relative to the 2:1 Cu: Ti molar ratio sample under identical reaction conditions. Finally, samples prepared without any prior N_2 annealing gave rise to improved activity readings as compared with their N_2 annealed counterparts. This finding could be ascribed to the formation and preponderance of active Cu sites in the guise of discrete

metallic islands immobilized on the external surfaces of the underlying core-shell motifs.

6. Acknowledgements

This material is based on work performed in SSW's laboratory, supported by the U.S. National Science Foundation under Grant No. CHE-1807640. Structural characterization experiments (TEM and SEM) for this manuscript were performed in part at the Center for Functional Nanomaterials, located at Brookhaven National Laboratory, which is supported by the U.S. Department of Energy under Contract No. DE-SC-00112704. We would also like to acknowledge the assistance of Dr. Luyao Li and Ivan Orozco in this work.

The catalytic activity measurements were carried out at the Chemistry Department of Brookhaven National Laboratory (BNL), and were supported by the Division of Chemical Science, Geosciences, and Bioscience of the Office of Basic Energy Sciences at the U.S. Department of Energy (DOE). This research also used resources associated with the 8-ID (ISS) and 7-BM (QAS) beamlines of the National Synchrotron Light Source II, a U.S. DOE Office of Science User Facility operated by BNL under Contract No. DE-SC0012704.

7. Supporting Information. Structural characterization data of as-prepared core-shell nanomaterials, involving changes in reaction parameters such as precursor, reaction time, and methodology of precursor addition; additional SEM-EDS measurements with quantitative analysis; TEM images of core-shell samples subjected to different pre-treatment and processing conditions; complementary XANES characterization of additional samples studied; catalytic activity results; and associated data tables (including comparison with prior literature studies).

References

(1) Olah, G. A.; Prakash, G. K. S.; Goeppert, A. Anthropogenic Chemical Carbon Cycle for a Sustainable Future. *J. Am. Chem. Soc.* **2011,** *133* (33), 12881-12898, DOI: 10.1021/ja202642y.
(2) Maeda, C.; Miyazaki, Y.; Ema, T. Recent Progress in Catalytic Conversions of Carbon Dioxide. *Catal. Sci.* **2014,** *4* (6), 1482-1497, DOI: 10.1039/C3CY00993A.
(3) Sakakura, T.; Choi, J.-C.; Yasuda, H. Transformation of Carbon Dioxide. *Chem. Rev.* **2007,** *107* (6), 2365-2387, DOI: 10.1021/cr068357u.
(4) Goeppert, A.; Czaun, M.; Jones, J.-P.; Surya Prakash, G. K.; Olah, G. A. Recycling of Carbon Dioxide to Methanol and Derived Products – Closing the Loop. *Chem. Soc. Rev.* **2014,** *43* (23), 7995-8048, DOI: 10.1039/C4CS00122B.
(5) Lu, Q.; Jiao, F. Electrochemical CO_2 Reduction: Electrocatalyst, Reaction Mechanism, and Process Engineering. *Nano Energy* **2016,** *29*, 439-456, DOI: 10.1016/j.nanoen.2016.04.009.
(6) Porosoff, M. D.; Yan, B.; Chen, J. G. Catalytic Reduction of CO_2 by H_2 for Synthesis of CO, Methanol and Hydrocarbons: Challenges and Opportunities. *Energy Environ. Sci.* **2016,** *9* (1), 62-73, DOI: 10.1039/C5EE02657A.
(7) Huang, P.; Ci, S.; Wang, G.; Jia, J.; Xu, J.; Wen, Z. High-Activity Cu Nanowires Electrocatalysts for CO_2 Reduction. *J. CO2 Util.* **2017,** *20*, 27-33, DOI: 10.1016/j.jcou.2017.05.002.
(8) Cao, L.; Raciti, D.; Li, C.; Livi, K. J. T.; Rottmann, P. F.; Hemker, K. J.; Mueller, T.; Wang, C. Mechanistic Insights for Low-Overpotential Electroreduction of CO_2 to CO on Copper Nanowires. *ACS Catal.* **2017,** *7* (12), 8578-8587, DOI: 10.1021/acscatal.7b03107.
(9) Ross, M. B.; Dinh, C. T.; Li, Y.; Kim, D.; De Luna, P.; Sargent, E. H.; Yang, P. Tunable Cu Enrichment Enables Designer Syngas Electrosynthesis from CO_2. *J. Am. Chem. Soc.* **2017,** *139* (27), 9359-9363, DOI: 10.1021/jacs.7b04892.
(10) Zhang, B.; Zhang, J. Rational Design of Cu-Based Electrocatalysts for Electrochemical Reduction of Carbon Dioxide. *J. Energy Chem.* **2017,** *26* (6), 1050-1066, DOI: 10.1016/j.jechem.2017.10.011.
(11) Jia, L.; Yang, H.; Deng, J.; Chen, J.; Zhou, Y.; Ding, P.; Li, L.; Han, N.; Li, Y. Copper-Bismuth Bimetallic Microspheres for Selective Electrocatalytic Reduction of CO_2 to Formate. *Chin. J. Chem* . **2019,** *37* (5), 497-500, DOI: 10.1002/cjoc.201900010.
(12) Zhu, W.; Zhang, L.; Yang, P.; Chang, X.; Dong, H.; Li, A.; Hu, C.; Huang, Z.; Zhao, Z.-J.; Gong, J. Morphological and Compositional Design of Pd–Cu Bimetallic Nanocatalysts with Controllable Product Selectivity toward CO_2 Electroreduction. *Small* **2018,** *14* (7), 1703314, DOI: 10.1002/smll.201703314.
(13) Barasa, G. O.; Yu, T.; Lu, X.; Zhou, X.; Wang, H.; Qian, L.; Yu, Y.; Liu, L.; Lei, P. Electrochemical Training of Nanoporous Cu-In catalysts for Efficient CO_2-to-CO Conversion and High Durability. *Electrochim. Acta* **2019,** *295*, 584-590, DOI: 10.1016/j.electacta.2018.10.175.
(14) Kortlever, R.; Shen, J.; Schouten, K. J.; Calle-Vallejo, F.; Koper, M. T. Catalysts and Reaction Pathways for the Electrochemical Reduction of Carbon Dioxide. *J Phys Chem Lett* **2015,** *6* (20), 4073-82, DOI: 10.1021/acs.jpclett.5b01559.
(15) Zhao, S.; Han, F.; Li, J.; Meng, X.; Huang, W.; Cao, D.; Zhang, G.; Sun, R.; Wong, C.-P. Advancements in Copper Nanowires: Synthesis, Purification, Assemblies, Surface Modification, and Applications. *Small* **2018,** *14* (26), 1800047, DOI: 10.1002/smll.201800047.
(16) Zhang, D.; Liu, P.; Xiao, S.; Qian, X.; Zhang, H.; Wen, M.; Kuwahara, Y.; Mori, K.; Li, H.; Yamashita, H. Microwave-Antenna Induced In Situ Synthesis of Cu Nanowire Threaded ZIF-8

with Enhanced Catalytic Activity in H_2 Production. *Nanoscale* **2016,** *8* (14), 7749-7754, DOI: 10.1039/C5NR07505J.
(17) Senanayake, S. D.; Stacchiola, D.; Rodriguez, J. A. Unique Properties of Ceria Nanoparticles Supported on Metals: Novel Inverse Ceria/Copper Catalysts for CO Oxidation and the Water-Gas Shift Reaction. *Acc. Chem. Res.* **2013,** *46* (8), 1702-1711, DOI: 10.1021/ar300231p.
(18) Senanayake, S. D.; Ramírez, P. J.; Waluyo, I.; Kundu, S.; Mudiyanselage, K.; Liu, Z.; Liu, Z.; Axnanda, S.; Stacchiola, D. J.; Evans, J.; Rodriguez, J. A. Hydrogenation of CO_2 to Methanol on CeO_x/Cu(111) and ZnO/Cu(111) Catalysts: Role of the Metal–Oxide Interface and Importance of Ce^{3+} Sites. *J. Phys. Chem. C* **2016,** *120* (3), 1778-1784, DOI: 10.1021/acs.jpcc.5b12012.
(19) Rodriguez, J. A.; Graciani, J.; Evans, J.; Park, J. B.; Yang, F.; Stacchiola, D.; Senanayake, S. D.; Ma, S.; Pérez, M.; Liu, P.; Sanz, J. F.; Hrbek, J. Water-Gas Shift Reaction on a Highly Active Inverse CeO_x/Cu(111) Catalyst: Unique Role of Ceria Nanoparticles. *Angew. Chem. Int. Ed.* **2009,** *48* (43), 8047-8050, DOI: 10.1002/anie.200903918.
(20) Kattel, S.; Ramírez, P. J.; Chen, J. G.; Rodriguez, J. A.; Liu, P. Active Sites for CO_2 Hydrogenation to Methanol on Cu/ZnO Catalysts. *Science* **2017,** *355* (6331), 1296, DOI: 10.1126/science.aal3573.
(21) Ciofini, I.; Le Bahers, T.; Adamo, C.; Odobel, F.; Jacquemin, D. Through-Space Charge Transfer in Rod-Like Molecules: Lessons from Theory. *J. Phys. Chem. C* **2012,** *116* (22), 11946-11955, DOI: 10.1021/jp3030667.
(22) Koenigsmann, C.; Santulli, A. C.; Gong, K.; Vukmirovic, M. B.; Zhou, W.-p.; Sutter, E.; Wong, S. S.; Adzic, R. R. Enhanced Electrocatalytic Performance of Processed, Ultrathin, Supported Pd–Pt Core–Shell Nanowire Catalysts for the Oxygen Reduction Reaction. *J. Am. Chem. Soc.* **2011,** *133* (25), 9783-9795, DOI: 10.1021/ja111130t.
(23) Koenigsmann, C.; Santulli, A. C.; Sutter, E.; Wong, S. S. Ambient Surfactantless Synthesis, Growth Mechanism, and Size-Dependent Electrocatalytic Behavior of High-Quality, Single Crystalline Palladium Nanowires. *ACS Nano* **2011,** *5* (9), 7471-7487, DOI: 10.1021/nn202434r.
(24) Koenigsmann, C.; Sutter, E.; Chiesa, T. A.; Adzic, R. R.; Wong, S. S. Highly Enhanced Electrocatalytic Oxygen Reduction Performance Observed in Bimetallic Palladium-Based Nanowires Prepared under Ambient, Surfactantless Conditions. *Nano Lett.* **2012,** *12* (4), 2013-2020, DOI: 10.1021/nl300033e.
(25) Liu, H.; Koenigsmann, C.; Adzic, R. R.; Wong, S. S. Probing Ultrathin One-Dimensional Pd–Ni Nanostructures As Oxygen Reduction Reaction Catalysts. *ACS Catal.* **2014,** *4* (8), 2544-2555, DOI: 10.1021/cs500125y.
(26) Liu, H.; An, W.; Li, Y.; Frenkel, A. I.; Sasaki, K.; Koenigsmann, C.; Su, D.; Anderson, R. M.; Crooks, R. M.; Adzic, R. R.; Liu, P.; Wong, S. S. In Situ Probing of the Active Site Geometry of Ultrathin Nanowires for the Oxygen Reduction Reaction. *J. Am. Chem. Soc.* **2015,** *137* (39), 12597-12609, DOI: 10.1021/jacs.5b07093.
(27) Koenigsmann, C.; Semple, D. B.; Sutter, E.; Tobierre, S. E.; Wong, S. S. Ambient Synthesis of High-Quality Ruthenium Nanowires and the Morphology-Dependent Electrocatalytic Performance of Platinum-Decorated Ruthenium Nanowires and Nanoparticles in the Methanol Oxidation Reaction. *ACS Appl. Mater. Interfaces* **2013,** *5* (12), 5518-5530, DOI: 10.1021/am4007462.

(28) Liu, H.; Adzic, R. R.; Wong, S. S. Multifunctional Ultrathin Pd_xCu_{1-x} and Pt~Pd_xCu_{1-x} One-Dimensional Nanowire Motifs for Various Small Molecule Oxidation Reactions. *ACS Appl. Mater. Interfaces* **2015,** *7* (47), 26145-26157, DOI: 10.1021/acsami.5b07964.
(29) Palomino, R. M.; Ramirez, P. J.; Liu, Z.; Hamlyn, R.; Waluyo, I.; Mahapatra, M.; Orozco, I.; Hunt, A.; Simonovis, J. P.; Senanayake, S. D.; Rodriguez, J. A. Hydrogenation of CO_2 on ZnO/Cu(100) and ZnO/Cu(111) Catalysts: Role of Copper Structure and Metal-Oxide Interface in Methanol Synthesis. *J. Phys. Chem. B* **2018,** *122* (2), 794-800, DOI: 10.1021/acs.jpcb.7b06901.
(30) Qian, F.; Lan, P. C.; Olson, T.; Zhu, C.; Duoss, E. B.; Spadaccini, C. M.; Han, T. Y.-J. Multiphase Separation of Copper Nanowires. *Chem. Commun.* **2016,** *52* (78), 11627-11630, DOI: 10.1039/C6CC06228H.
(31) Mondal, K.; Sharma, A. Recent Advances in the Synthesis and Application of Photocatalytic Metal–Metal Oxide Core–Shell Nanoparticles for Environmental Remediation and Their Recycling Process. *RSC Adv.* **2016,** *6* (87), 83589-83612, DOI: 10.1039/C6RA18102C.
(32) Liu, X.; Iocozzia, J.; Wang, Y.; Cui, X.; Chen, Y.; Zhao, S.; Li, Z.; Lin, Z. Noble Metal–Metal Oxide Nanohybrids with Tailored Nanostructures for Efficient Solar Energy Conversion, Photocatalysis and Environmental Remediation. *Energy Environ. Sci.* **2017,** *10* (2), 402-434, DOI: 10.1039/C6EE02265K.
(33) Xiao, S.; Liu, P.; Zhu, W.; Li, G.; Zhang, D.; Li, H. Copper Nanowires: A Substitute for Noble Metals to Enhance Photocatalytic H_2 Generation. *Nano Lett.* **2015,** *15* (8), 4853-4858, DOI: 10.1021/acs.nanolett.5b00082.
(34) Liu, D.; Wu, B.; Mubeen, S.; Ding, K.; Zeng, H.; Chuong, T. T.; Moskovits, M.; Stucky, G. D. Microwave-Assisted Synthesis of Ultrastable Cu@TiO_2 Core-Shell Nanowires with Tunable Diameters via a Redox-Hydrolysis Synergetic Process. *ChemNanoMat* **2018,** *4* (9), 914-918, DOI: 10.1002/cnma.201800210.
(35) Babu, B.; Mallikarjuna, K.; Reddy, C. V.; Park, J. Facile Synthesis of Cu@TiO_2 Core Shell Nanowires for Efficient Photocatalysis. *Mater. Lett.* **2016,** *176*, 265-269, DOI: 10.1016/J.MATLET.2016.04.146.
(36) Zhang, Y.; Zhou, N.; Zhang, K.; Yan, F. Plasmonic Copper Nanowire@TiO_2 Nanostructures for Improving the Performance of Dye-Sensitized Solar Cells. *J. Power Sources* **2017,** *342*, 292-300, DOI: 10.1016/j.jpowsour.2016.12.068.
(37) Chen, C.; Pang, Y.; Zhang, F.; Zhong, J.; Zhang, B.; Cheng, Z. Sharp Cu@Sn Nanocones on Cu Foam for Highly Selective and Efficient Electrochemical Reduction of CO_2 to Formate. *J. Mater. Chem. A* **2018,** *6* (40), 19621-19630, DOI: 10.1039/c8ta06826g.
(38) Hu, H.; Wang, Y.; Du, N.; Sun, Y.; Tang, Y.; Hu, Q.; Wan, P.; Dai, L.; Fisher, A. C.; Yang, X. J. Thermal-Treatment-Induced Cu−Sn Core/Shell Nanowire Array Catalysts for Highly Efficient CO_2 Electroreduction. *ChemElectroChem* **2018,** *5* (24), 3854-3858, DOI: 10.1002/celc.201801267.
(39) Xie, H.; Chen, S.; Ma, F.; Liang, J.; Miao, Z.; Wang, T.; Wang, H.-L.; Huang, Y.; Li, Q. Boosting Tunable Syngas Formation via Electrochemical CO_2 Reduction on Cu/In_2O_3 Core/Shell Nanoparticles. *ACS Appl. Mater. Interfaces* **2018,** *10* (43), 36996-37004, DOI: 10.1021/acsami.8b12747.
(40) Li, Q.; Fu, J.; Zhu, W.; Chen, Z.; Shen, B.; Wu, L.; Xi, Z.; Wang, T.; Lu, G.; Zhu, J.-j.; Sun, S. Tuning Sn-Catalysis for Electrochemical Reduction of CO_2 to CO via the Core/Shell Cu/SnO_2 Structure. *J. Am. Chem. Soc.* **2017,** *139* (12), 4290-4293, DOI: 10.1021/jacs.7b00261.

(41) Schreier, M.; Héroguel, F.; Steier, L.; Ahmad, S.; Luterbacher, J. S.; Mayer, M. T.; Luo, J.; Grätzel, M. Solar Conversion of CO_2 to CO using Earth-Abundant Electrocatalysts Prepared by Atomic Layer Modification of CuO. *Nat. Energy* **2017,** *2* (7), 1-9, DOI: 10.1038/nenergy.2017.87.
(42) Monz. Enhanced Electrocatalytic Activity of Au@Cu Core@Shell Nanoparticles towards CO_2 Reduction. *J. Mater. Chem. A* **2015,** *3* (47), 23690--23698, DOI: 10.1039/c5ta06804e.
(43) Das, S.; Pérez-Ramírez, J.; Gong, J.; Dewangan, N.; Hidajat, K.; Gates, B. C.; Kawi, S. Core–Shell Structured Catalysts for Thermocatalytic, Photocatalytic, and Electrocatalytic Conversion of CO_2. *Chem. Soc. Rev.* **2020**, DOI: 10.1039/C9CS00713J.
(44) Tigan, D.; Genlik, S. P.; Imer, B.; Unalan, H. E. Core/Shell Copper Nanowire Networks for Transparent Thin Film Heaters. *Nanotechnology* **2019,** *30* (32), 325202, DOI: 10.1088/1361-6528/ab19c6.
(45) Cao, F.-F.; Xin, S.; Guo, Y.-G.; Wan, L.-J. Wet Chemical Synthesis of Cu/TiO_2 Nanocomposites with Integrated Nano-Current-Collectors as High-Rate Anode Materials in Lithium-Ion Batteries. *Phys. Chem. Chem. Phys.* **2011,** *13* (6), 2014-2020, DOI: 10.1039/C0CP01119C.
(46) Wang, H.; Wu, C.; Huang, Y.; Sun, F.; Lin, N.; Soomro, A. M.; Zhong, Z.; Yang, X.; Chen, X.; Kang, J.; Cai, D. One-Pot Synthesis of Superfine Core–Shell Cu@metal Nanowires for Highly Tenacious Transparent LED Dimmer. *ACS Appl. Mater. Interfaces* **2016,** *8* (42), 28709-28717, DOI: 10.1021/acsami.6b09009.
(47) Bilecka, I.; Niederberger, M. Microwave Chemistry for Inorganic Nanomaterials Synthesis. *Nanoscale* **2010,** *2* (8), 1358-1358, DOI: 10.1039/b9nr00377k.
(48) Zhu, Y.-J.; Chen, F. Microwave-Assisted Preparation of Inorganic Nanostructures in Liquid Phase. *Chem. Rev.* **2014,** *114* (12), 6462-6555, DOI: 10.1021/cr400366s.
(49) Niu, J.; Yao, B.; Peng, C.; Zhang, W.; Chen, Y. Rapid Microwave Hydrothermal Methods Synthesis of TiO_2 Photocatalysts Using Different Sources of Materials. *Integr. Ferroelectr.* **2014,** *152* (1), 163-173, DOI: 10.1080/10584587.2014.902276.
(50) Periyat, P.; Leyland, N.; McCormack, D. E.; Colreavy, J.; Corr, D.; Pillai, S. C. Rapid Microwave Synthesis of Mesoporous TiO_2 for Electrochromic Displays. *J. Mater. Chem.* **2010,** *20* (18), 3650-3655, DOI: 10.1039/B924341K.
(51) Scofield, M. E.; Koenigsmann, C.; Bobb-Semple, D.; Tao, J.; Tong, X.; Wang, L.; Lewis, C. S.; Vukmirovic, M. B.; Zhu, Y.; Adzic, R. R.; Wong, S. S. Correlating the Chemical Composition and Size of Various Metal Oxide Substrates with the Catalytic Activity and Stability of As-Deposited Pt Nanoparticles for the Methanol Oxidation Reaction. *Catal. Sci.* **2016,** *6* (7), 2435-2450, DOI: 10.1039/C5CY01444A.
(52) Khatim, O.; Amamra, M.; Chhor, K.; Bell, A. M. T.; Novikov, D.; Vrel, D.; Kanaev, A. Amorphous–Anatase Phase Transition in Single Immobilized TiO_2 Nanoparticles. *Chem. Phys. Lett.* **2013,** *558*, 53-56, DOI: 10.1016/j.cplett.2012.12.019.
(53) Kyriakou, V.; Vourros, A.; Garagounis, I.; Carabineiro, S. A. C.; Maldonado-Hódar, F. J.; Marnellos, G. E.; Konsolakis, M. Highly Active and Stable TiO_2-Supported Au Nanoparticles for CO_2 Reduction. *Catal. Commun.* **2017,** *98*, 52-56, DOI: 10.1016/j.catcom.2017.05.003.
(54) Fisher, I. A.; Bell, A. T. In-Situ Infrared Study of Methanol Synthesis from H_2/CO_2 over Cu/SiO_2 and Cu/ZrO_2/SiO_2. *J. Catal.* **1997,** *172* (1), 222-237, DOI: 10.1006/jcat.1997.1870.
(55) Hand, M. R.; Holloway, S. A Theoretical Study of the Dissociation of H_2/Cu. *J. Chem. Phys.* **1989,** *91* (11), 7209-7219, DOI: 10.1063/1.457288.

(56) Nakamura, J.; Rodriguez, J. A.; Campbell, C. T. Does CO_2 Dissociatively Adsorb on Cu Surfaces? *J. Phys.: Condens. Matter* **1989,** *1* (SB), SB149-SB160, DOI: 10.1088/0953-8984/1/sb/026.
(57) Mino, L.; Spoto, G.; Ferrari, A. M. CO_2 Capture by TiO_2 Anatase Surfaces: A Combined DFT and FTIR Study. *Journal of Physical Chemistry C* **2014,** *118* (43), 25016-25026, DOI: 10.1021/jp507443k.
(58) Chen, H.-Y. T.; Tosoni, S.; Pacchioni, G. Hydrogen Adsorption, Dissociation, and Spillover on Ru_{10} Clusters Supported on Anatase TiO_2 and Tetragonal ZrO_2 (101) Surfaces. *ACS Catal.* **2015,** *5* (9), 5486-5495, DOI: 10.1021/acscatal.5b01093.

Figure Captions

Figure 1. (A) XRD pattern of the Cu@TiO_2 core/shell structure (black), referenced to the standard JCPDS database #03-1018 (red). (B) SEM and (C-D) HRTEM images highlighting the TiO_2 coating onto the underlying Cu NWs, generated using a microwave method. The analyzed sample was prepared by heating a 1 Cu: 2 Ti molar ratio solution to 150°C for 30 minutes. The anatase TiO_2 *d*-spacing for the (101) plane has been correspondingly indexed.

Figure 2. Example of (A) an EDX elemental spectrum and its corresponding (B) SEM image, wherein the black box highlights the area in which the EDX data were acquired of as-prepared Cu/TiO_2 core/shell architectures, shown in Figure 1 (i.e., the 1Cu@2TiO_2 sample). Both of the expected Cu and Ti elemental signals appear to be present within the images.

Figure 3. SEM and HRTEM images associated with various TiO_2 shell sizes within a series of Cu@TiO_2 architecture, in which the TBOT amount was systematically varied from (A, D, G, J) 0.05 mL TBOT, (B, E, H, K) 0.025 mL TBOT, to (C, F, I, L) 0.0125 mL TBOT. The purple bracket highlights the TiO_2 'shell', whereas the red bracket delineates the Cu 'core'.

Figure 4. Correlating the resulting titania shell size with the initial Ti precursor amounts used.

Figure 5. TEM images of Cu@TiO_2 core@shell motifs, possessing (A, C, E, G) a 2: 1 molar ratio and (B, D, F, H) a 1: 2 Cu: Ti molar ratio, respectively. Samples were observed after (A, B) N_2 treatment, (C, D) an O_2 treatment, and (E, F) a H_2 treatment, respectively. Samples were also analyzed (G, H) after the CO_2 reaction process itself.

Figure 6. (A) Normalized catalytic activity (in $\mu mol*(s*g_{Cu})^{-1}$) for Cu@TiO_2 samples in the presence of N_2 annealing coupled with data associated with the corresponding Cu NW controls. (B) Corresponding XANES data obtained under different pre-treatment conditions: the pristine 1Cu@2TiO_2 sample (black), sample annealed in N_2 at 450^oC (red), followed by treatment with

O_2 at 350°C (10 vol % of O_2 / N_2 for 1 hour) (blue), with subsequent processing in H_2 at 450°C (10 vol % of H_2 / N_2 at 450°C for 1 hour) (green).

Figure 7. Prior to the CO_2 hydrogenation reaction. (A and B) TEM images, (C) HRTEM image, and (D-G) HRTEM-EDAX spectra of Cu@TiO_2 core@shell motifs, characterized by a 1: 2 Cu: Ti molar ratio, after heat treatment but without any N_2 annealing. Elemental distributions of (E) Cu, (F) O, and (G) Ti elements are shown with an overlay of these signals presented in (D). Scale bars for HRTEM images are set to 250 nm.

Figure 8. After the CO_2 hydrogenation reaction. (A and B) TEM images, (C) HRTEM image, and (D-G) HRTEM-EDAX spectra of Cu@TiO_2 core@shell motifs, characterized by a 1: 2 Cu: Ti molar ratio, after heat treatment but without any N_2 annealing. Elemental distributions of (E) Cu, (F) O, and (G) Ti elements are shown with an overlay of these signals presented in (D). Scale bars for HRTEM images are set to 250 nm.

Figure 9. (A) Normalized catalytic activity (in $\mu mol*(s*g_{Cu})^{-1}$) for Cu@TiO_2 samples in the absence of any N_2 annealing coupled with data associated with the corresponding Cu NW controls. (B) Corresponding XANES data taken under different pre-treatment conditions: pristine 1Cu@2TiO_2 sample (black), followed by processing with O_2 at 350°C (10 vol % of O_2 / N_2 for 1 hour) (red), with a subsequent treatment in H_2 at 450°C (10 vol % of H_2 / N_2 at 450°C for 1 hour) (blue).

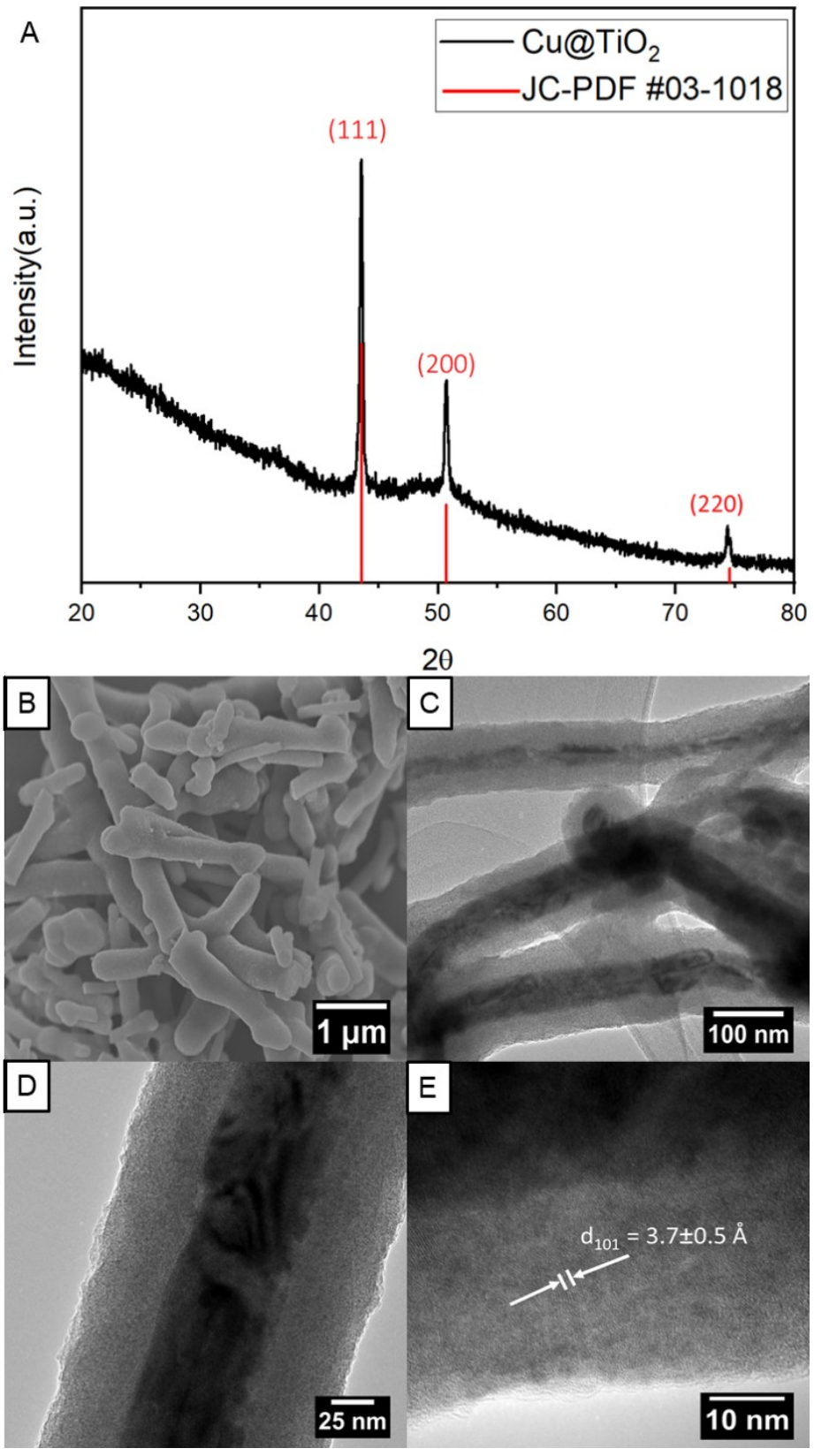
A
Cu@TiO2
JC-PDF #03-1018
(111)
(200)
(220)
Intensity(a.u.)
20
30
40
50
60
70
80
2θ
B
1 μm
C
100 nm
D
25 nm
E
d101 = 3.7±0.5 Å
10 nm

Figure 1.

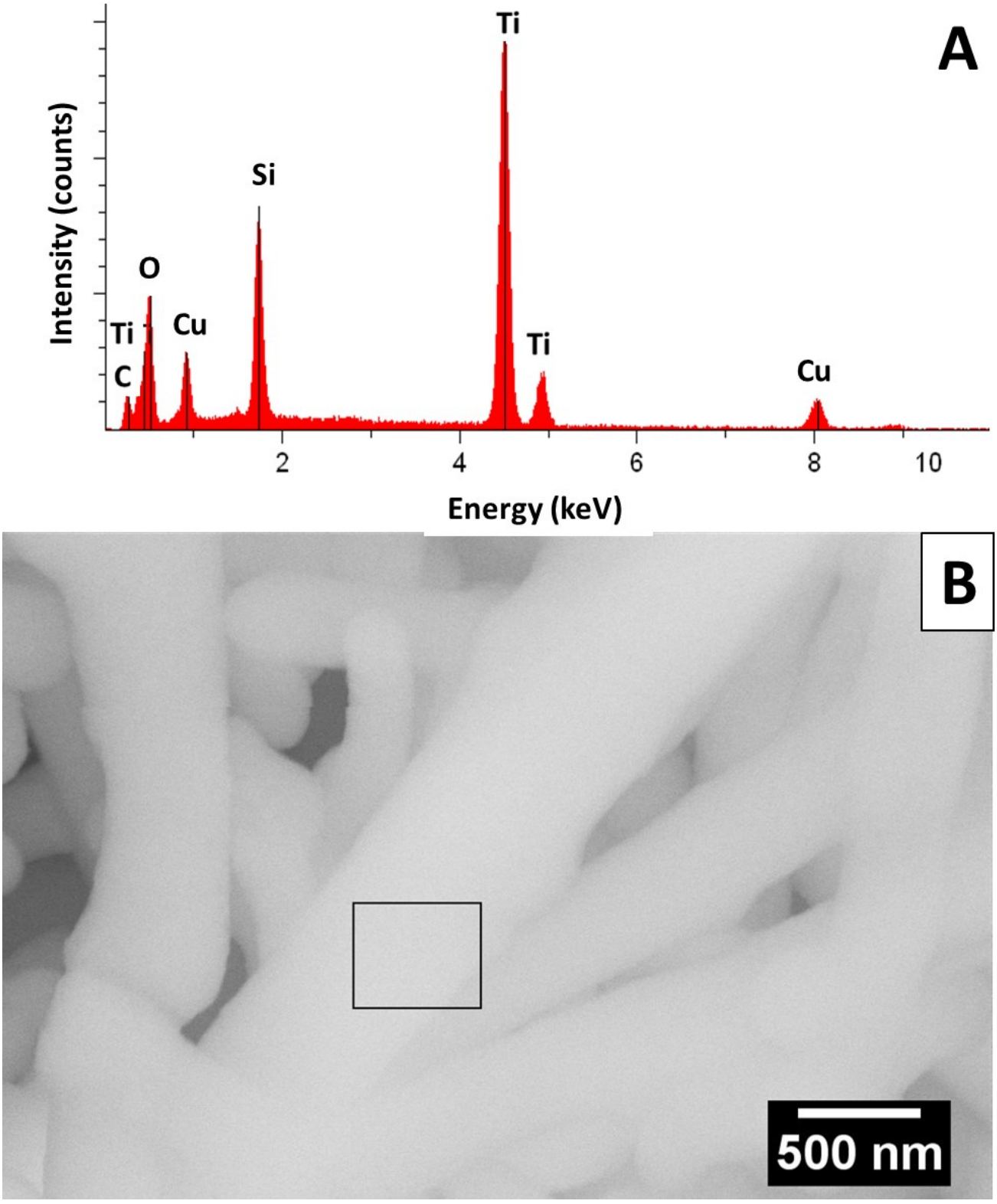
A
Intensity (counts)
Ti
O
Cu
Ti
C
Si
Ti
Ti
Cu
2
4
6
8
10
Energy (keV)
B
500 nm

Figure 2.

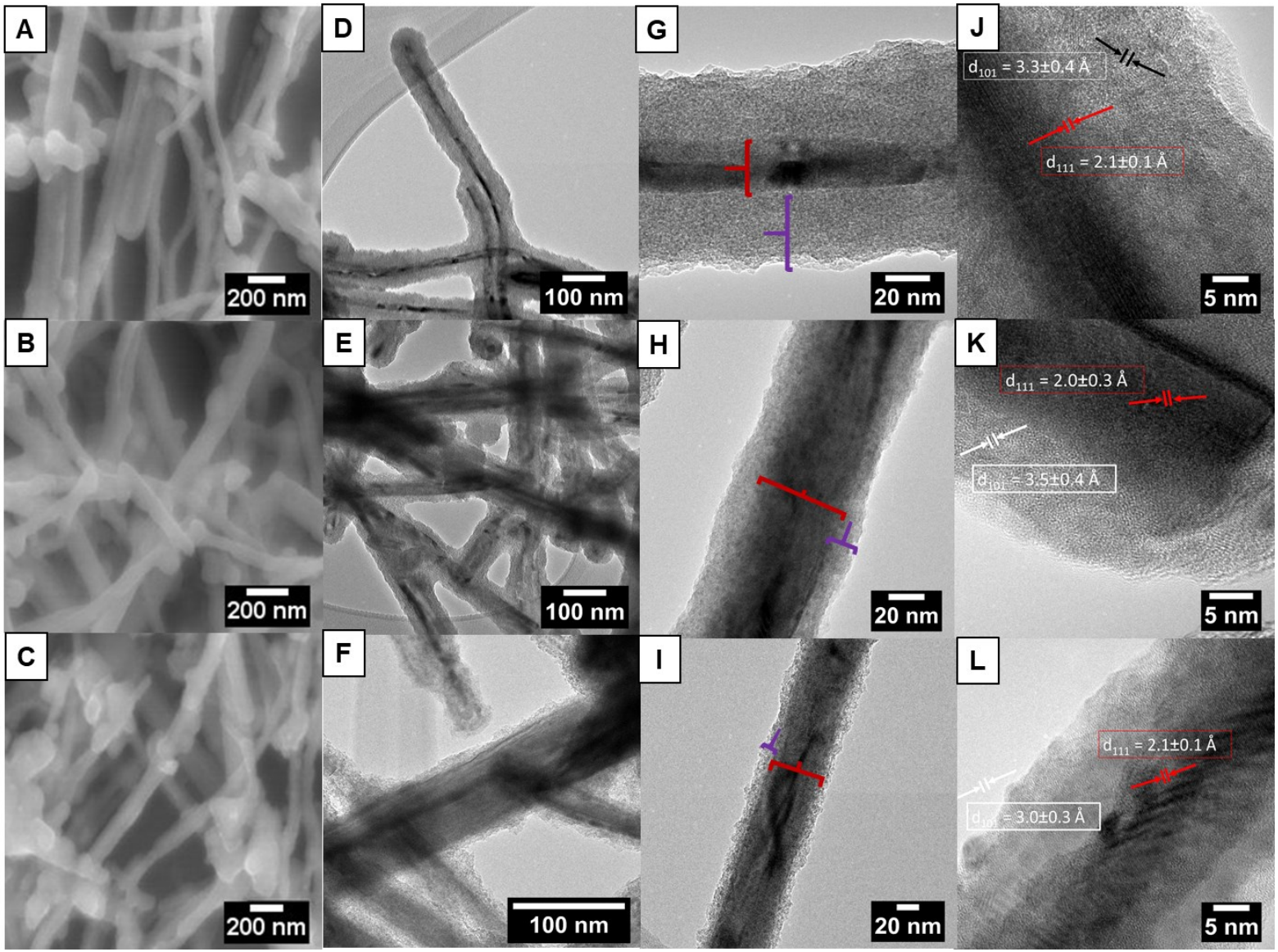
A
200 nm
D
100 nm
G
20 nm
J
d101 = 3.3±0.4 Å
d111 = 2.1±0.1 Å
5 nm
B
200 nm
E
100 nm
H
20 nm
K
d111 = 2.0±0.3 Å
d101 = 3.5±0.4 Å
5 nm
C
200 nm
F
100 nm
I
20 nm
L
d111 = 2.1±0.1 Å
5 nm

Figure 3.

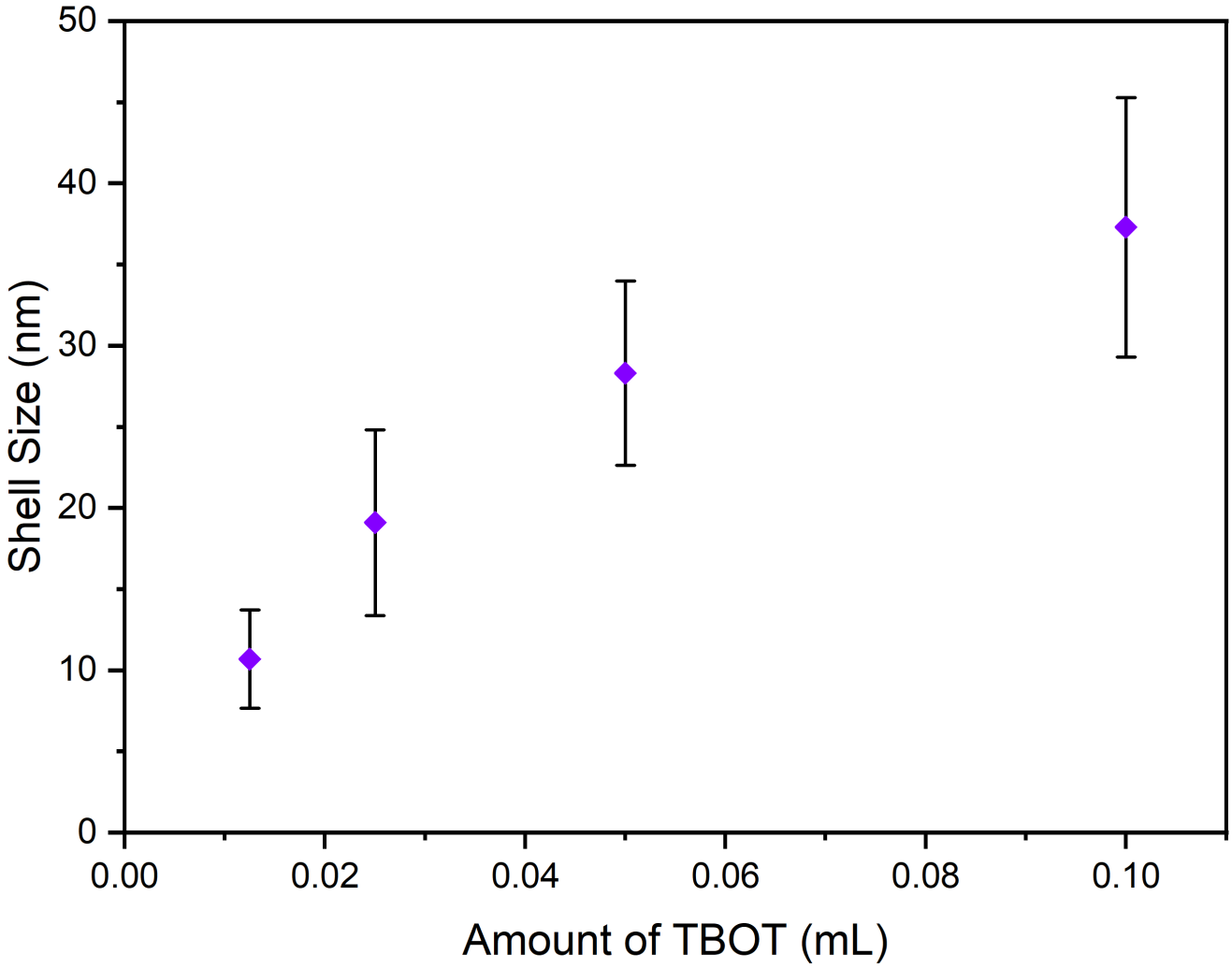
Shell Size (nm)
Amount of TBOT (mL)
0
10
20
30
40
50
0.00
0.02
0.04
0.06
0.08
0.10

Figure 4.

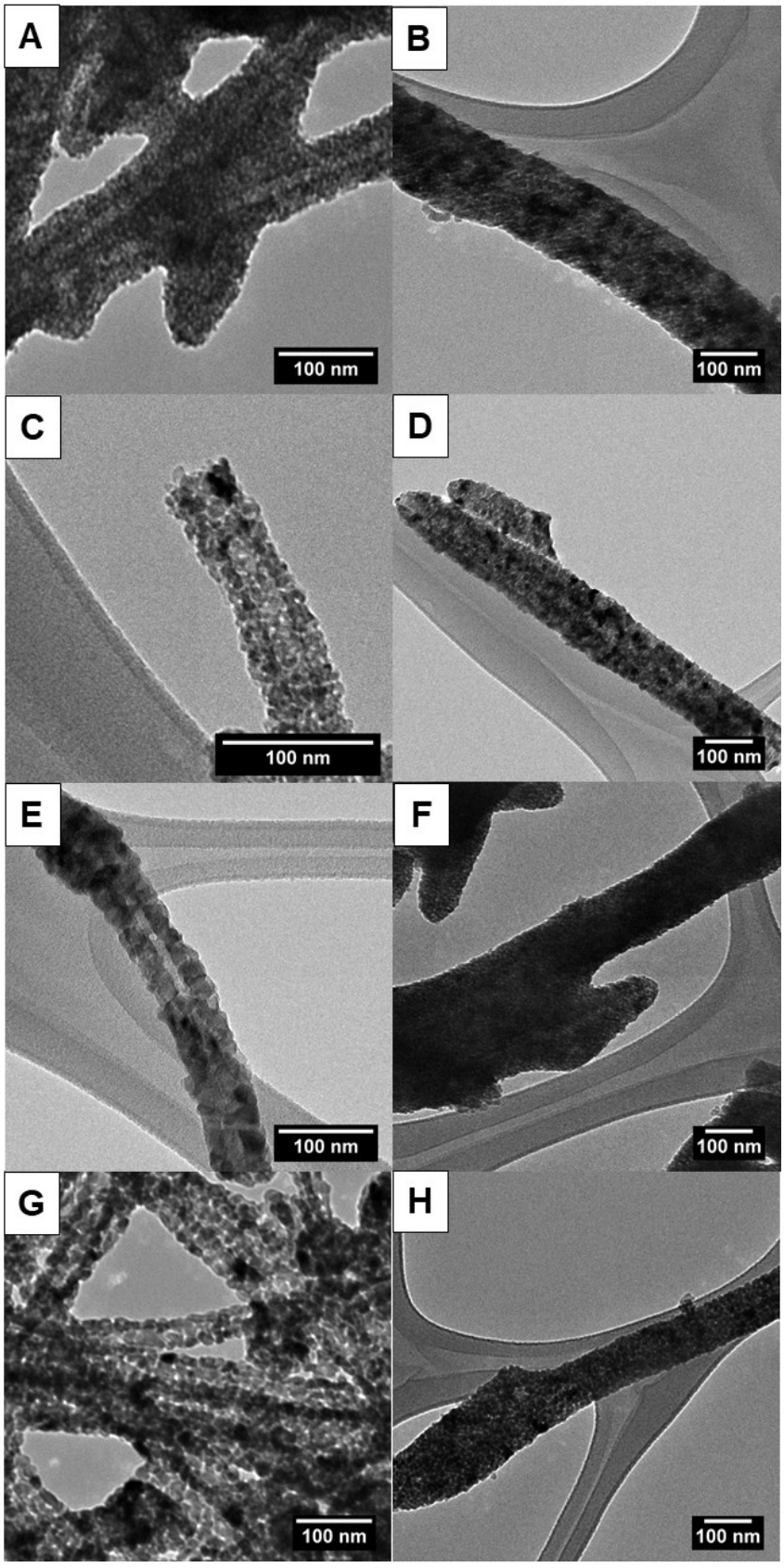

Figure 5.

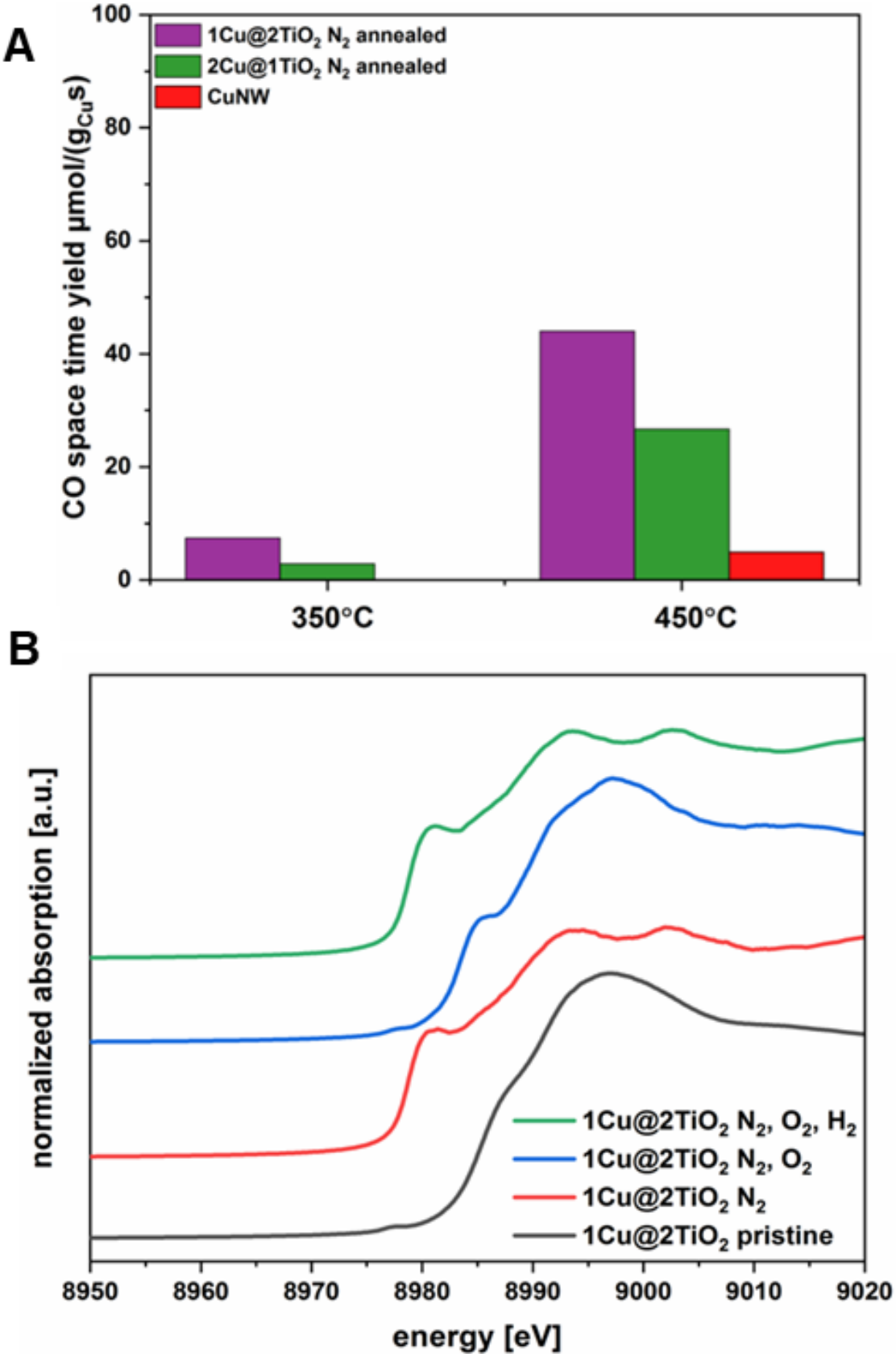
A
1Cu@2TiO2 N2 annealed
2Cu@1TiO2 N2 annealed
CuNW
CO space time yield µmol/(gCus)
100
80
60
40
20
0
350°C
450°C
B
normalized absorption [a.u.]
1Cu@2TiO2 N2, O2, H2
1Cu@2TiO2 N2, O2
1Cu@2TiO2 N2
1Cu@2TiO2 pristine
8950
8960
8970
8980
8990
9000
9010
9020
energy [eV]

Figure 6.

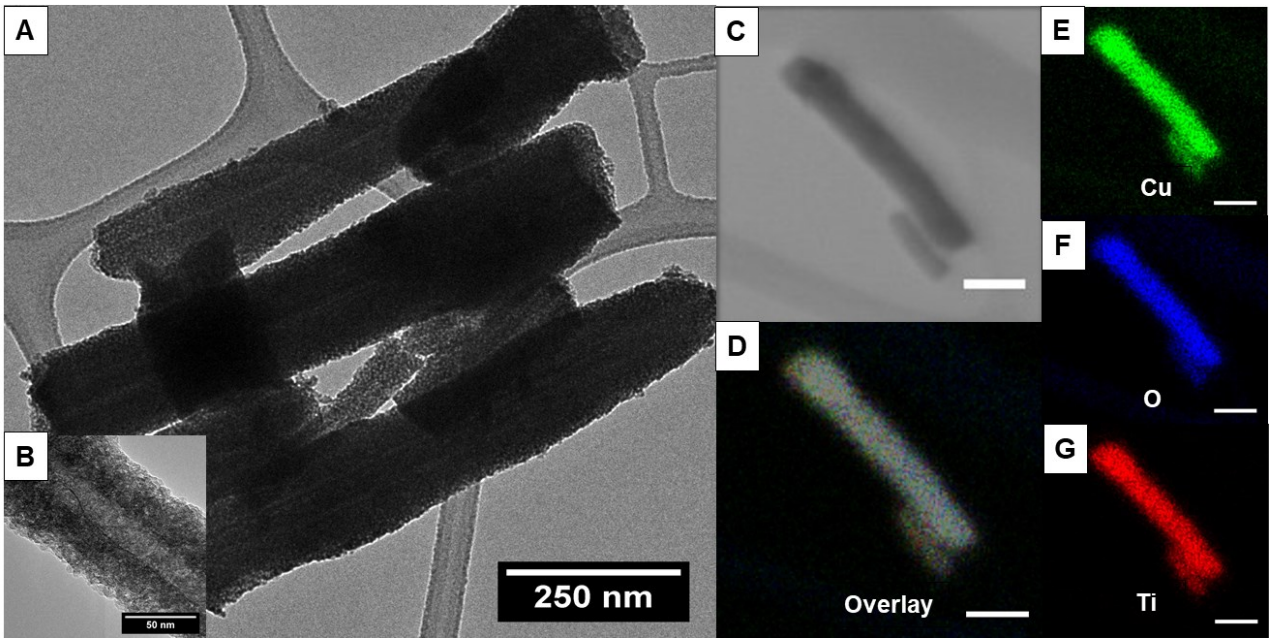

Figure 7.

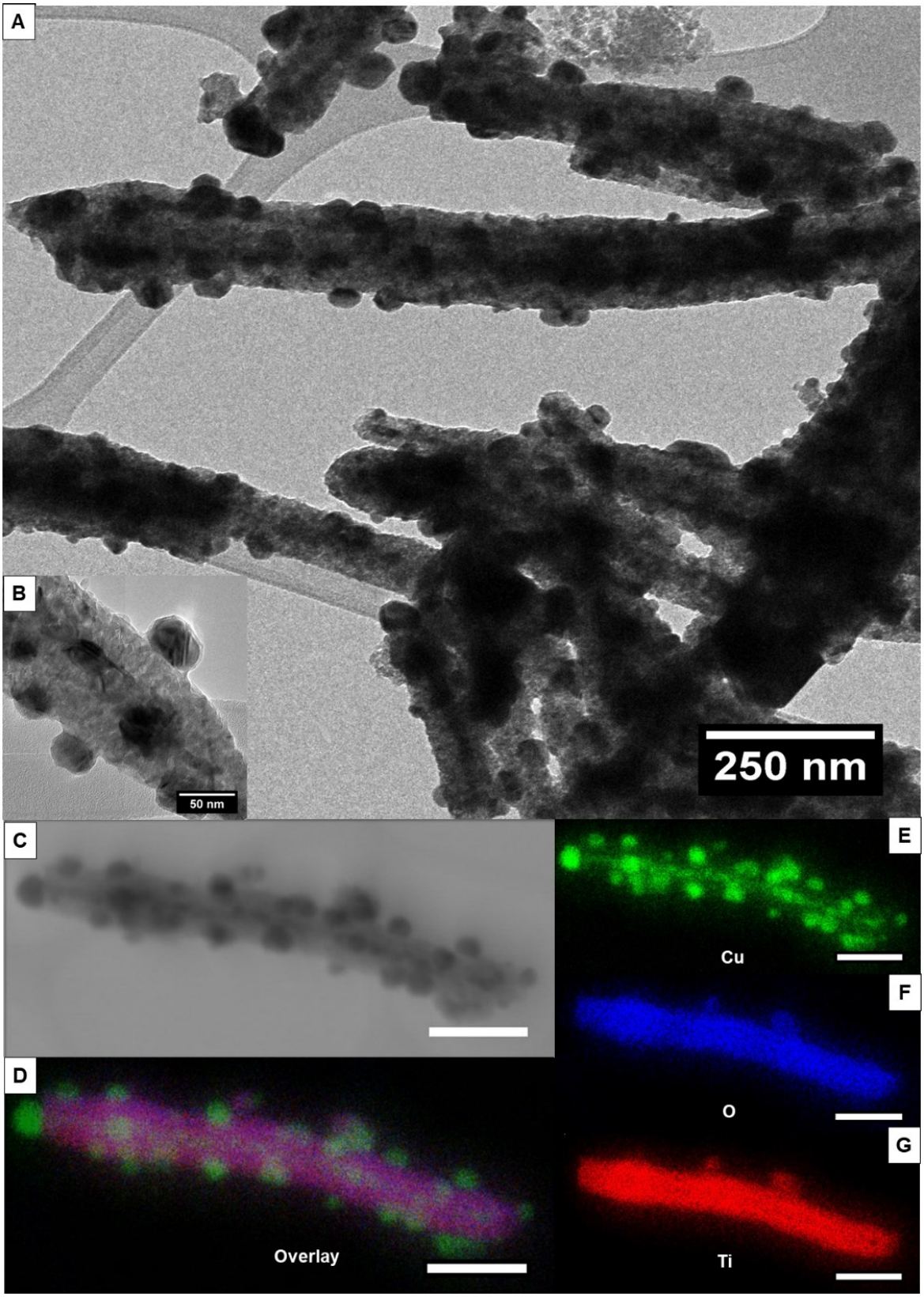

Figure 8.

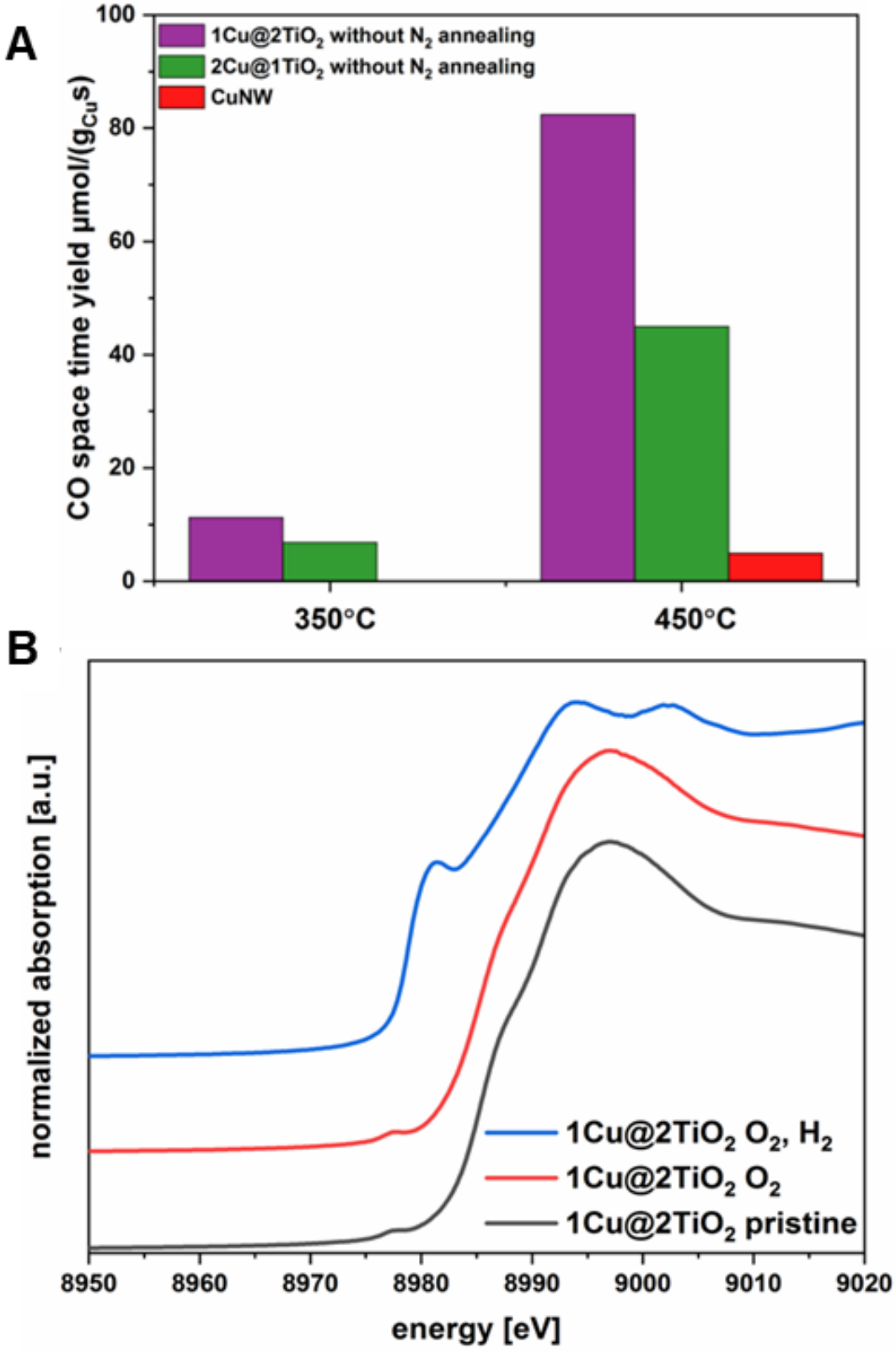
A
100
80
60
40
20
0
CO space time yield µmol/(g$_{Cu}$s)
1Cu@2TiO$_2$ without N$_2$ annealing
2Cu@1TiO$_2$ without N$_2$ annealing
CuNW
350°C
450°C
B
normalized absorption [a.u.]
1Cu@2TiO$_2$ O$_2$, H$_2$
1Cu@2TiO$_2$ O$_2$
1Cu@2TiO$_2$ pristine
8950
8960
8970
8980
8990
9000
9010
9020
energy [eV]

Figure 9.

Table 1. Summary of Quantitative Results derived from TEM and HRTEM Images.

TBOT Amount (mL)	Molar Ratio of Cu: Ti	Measured Shell Radius (nm)	Cu d_{111}(Å)	TiO_2 d_{101} (Å)
0.1	1: 2	37.3 ± 8.0	N/A	3.7 ± 0.5
0.05	1: 1	28.3 ± 5.7	2.1 ± 0.1	3.3 ± 0.4
0.025	2: 1	19.1 ± 5.7	2.0 ± 0.3	3.5 ± 0.4
0.0125	4: 1	10.7 ± 3.0	2.1 ± 0.1	3.0 ± 0.3

Table 2. Summary of Quantitative Results Obtained from TEM and HRTEM Images.

Molar Ratio Cu: Ti	Initial Radius (nm)	Radius After N_2 Treatment (nm)	Radius After N_2 Followed by O_2 Treatment (nm)	Radius After N_2 Then by O_2 Then H_2 Treatments (nm)	Radius After N_2 Then by O_2 Then by H_2 Treatments After Reaction (nm)	Radius After O_2 Treatment (nm)	Radius After O_2 Then by H_2 Treatments (nm)	Radius After O_2 Then by H_2 Treatments After Reaction (nm)
1: 2	37.3 ± 8.0	39.1 ± 6.9	39.6 ± 11.6	39.3 ± 6.3	37.8 ± 9.2	48.5 ± 6.3	49.8 ± 11.1	34.1 ± 2.1
2: 1	19.1 ± 5.7	26.8 ± 7.4	26.3 ± 6.5	22.3 ± 7.7	15.8 ± 3.7	18.7 ± 4.7	20.6 ± 3.3	18.6 ± 3.2

Table 3. Catalytic activity values for CO_2 Reduction in μmol/(g_{Cu}s).

With N_2 annealing	1Cu@2TiO_2	2Cu@1TiO_2	Cu NW
350°C	7.4	2.8	0
450°C	44	27	4.9
Without N_2 annealing	**1Cu@2TiO_2**	**2Cu@1TiO_2**	**Cu NW**
350C	11	6.8	0
450C	82	45	4.9

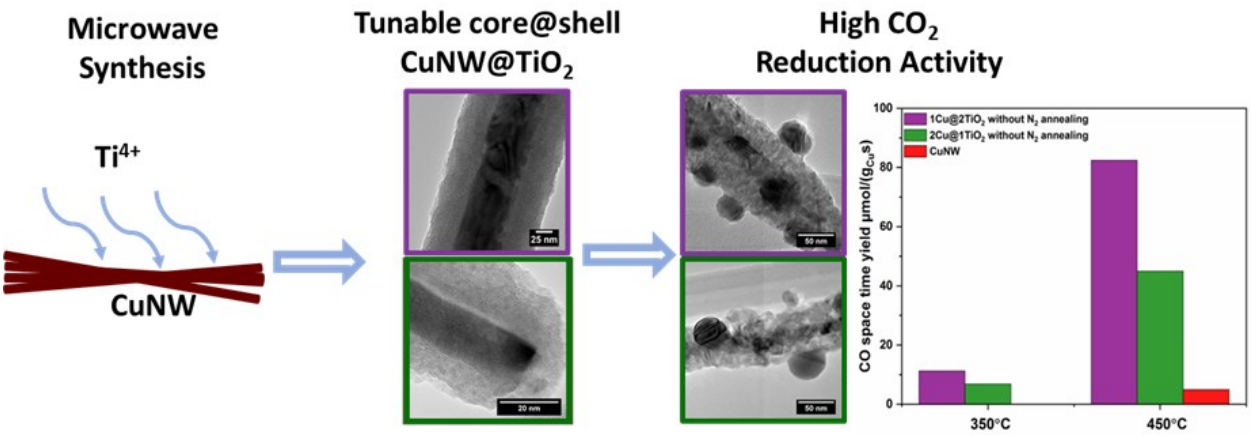

TOC Figure. Microwave process used to form tunable Cu@TiO_2 nanowire core@shell motifs for enhanced CO_2 reduction performance.